

Chapter 4. Description and Validation of Predicted Structure for LPA₂

4.1. Introduction

This chapter presents the computed structure and morphology of LPA₂ with selected ligands obtained through the methods described in Chapter 3. Section 4.2 describes the structure of the transmembrane region of LPA₂ and draws parallels to the crystal structure of bovine rhodopsin (BR). Section 4.3 identifies the binding mode of 1-oleoyl LPA and other species of LPA with different lipid tails. Section 4.4 validates the modeled structure by comparing the experimental activation data of a family of stereoisomeric LPA mimetics to our predicted binding energies. Section 4.5 describes the results from the full system molecular dynamics. This chapter relies heavily on table- and figure-based presentation of the data. For simplicity, Section 4.6 contains all tables and figures for this chapter.

4.2. Structure of LPA₂

As outlined in Chapter 3, TM2ndS determines which residues belong to the expected transmembrane helices. For LPA₂, TM2ndS successfully predicts seven hydrophobic regions without modification of the window size or other input parameters. Figure 4.1 plots the computed hydrophobicity of each residue in LPA₂ against the residue position in the protein's sequence. A global baseline adjustment (dotted line) resolves the hydrophobic regions assigned to the putative helices. As expected from research on other Class A GPCRs, each helix is 20-30 residues long and contains the appropriate conserved

residue(s) (Table 4.1). The hydrophobic centers calculated for each predicted helix define a reasonable plane for the center of the cellular membrane, as demonstrated by the minimal translation seen in the long time-scale dynamics.

Following the putative structure assignment, rotating the helices optimizes the protein structure. Rotating each helix minimizes the exposure of hydrophilic residues to the lipid membrane while maximizing inter-helical interactions. Following this optimization, the LPA₂ bundle shows inter-helical hydrogen bonds between helices 1 and 2, 1 and 7, 2 and 3, 2 and 7, 3 and 4, 3 and 5, 4 and 5, as well as 6 and 7. Table 4.2 lists the hydrogen bonds and their distances from heavy atom to heavy atom after the original helical optimization of the bundle.

The hydrogen bonds seen in our model favorably compare to what is known about GPCR structures from the crystal structure of rhodopsin.¹ As an example, Figure 4.2 shows the hydrogen bonding network between helices 1, 2, and 7 is very similar in both structures. In addition to these similarities, our predicted structure shows inter-helical hydrogen bonding similar to the homology models previously developed for the *edg* receptors.

Beyond the conserved hydrogen bond networks seen in the transmembrane (TM) bundle, our methods also allow each helix to relax. Helices containing prolines develop the curvature that one would expect based on general protein structure trends. In particular, there are conserved prolines in TM4 and helix 6 in LPA₂ and rhodopsin. Both of those helices, in LPA₂, developed natural kinks prior to packing of the full bundle during the all-atom molecular dynamics relaxation of each individual helix. Figure 4.3 overlays the LPA₂ transmembrane region, after optimization of the bundle, on the TM

region of the rhodopsin crystal structure (primary accession number: 1F88). Although we utilize the topology seen in a low-resolution crystal structure of rhodopsin, the optimized helices in LPA₂ reorient themselves with unique tilts. The root-mean-squared deviation of the C-alpha carbons in the TM bundles is 6.42 Å, indicating that these protein structures have significant differences. With such dramatic structural differences, one must carefully examine results from homology models, as they may contain artifacts from the constraints implicit in the choice of template structure. First principles structure prediction methods, like the procedure used in this work, allow for differences between proteins to evolve organically.

Although there are significant differences in the orientations of the helical backbones between proteins, the most highly conserved residues in the GPCR family strongly overlap in TM regions 1, 2, and 6 (Figure 4.4). LPA₂ does not have the proline residues in helices 5 or 7 that are seen in rhodopsin. The LPA₂ residue that is aligned with the proline in a sequence alignment of helix 7 (alanines) has similar structural alignment with respect to translation.

Helices 3, 4, and 7 show very good overlap with respect to translation. However, upon rotating the structures, we note different orientations for those helices. This is particularly interesting because the binding site for retinal in rhodopsin lies in the pocket surrounded by helices 3, 4, and 5. Our docking studies demonstrate binding of LPA in that same region within LPA₂.

Even without using experimental data, the present structure prediction technique replicates many of the structural traits seen in rhodopsin, including hydrogen-bonding networks, relative translation of the helices and, in many cases, relative rotational

orientation of the helices. As an additional advantage, this procedure allows rapid exploration of differences between proteins without intense computational effort.

4.3. Prediction of Putative Binding Sites

The hypothesis of this study is that binding of ligands in all GPCRs is dominated by binding within the transmembrane region. The method seeks to explore the widest possible parameter space for ligand binding in order to find the optimal docking configuration. Therefore, we “alanize” the bundle, creating significantly more space for the lipid tail of the endogenous ligand to dock. Prior to this alanizing, docking attempts had very little success creating complexes with buried ligands (data not shown).

PASS creates seven sphere sets for docking, shown in Figure 4.5. Six of the sphere regions are located significantly inside the transmembrane barrel, but all seven sphere sets were used for docking the LPA *cis*-18:1 ligand into LPA₂. We did not utilize a diversity threshold in our sampling of the TM barrel, yet the anchor search sampling of the TM barrel was quite thorough (Figure 4.6).

After adding loops to the ligand-protein complex, the final lowest energy structure of LPA *cis*-18:1 docked into LPA₂ shows protein-ligand hydrogen bonds between the phosphate head of LPA and two polar residues on TM 3. Using the GPCR residue identification scheme developed by Ballesteros and Weinstein, these residues are denoted Q3.29 and R3.28. For reference, this identification scheme gives the number of the helix first, followed by the location of a residue relative to most highly conserved residue in that helix, which is labeled X.50. The sequential designations for these residues are R¹⁰⁷ and Q¹⁰⁸. The distance between Q3.29 and the phosphate head is 2.88 Å, while R3.28

has polar contacts with all three exposed oxygen atoms on the phosphate head, as seen in Figure 4.7 with distances of 2.86, 2.86, and 3.12 Å. Previous modeling studies and site-directed mutagenesis experiments on S1P₁, LPA₁, and LPA₃ implicate both the glutamine and arginine that contact the phosphate head in the binding of agonists.²⁻⁴ The arginine is conserved through the entire *edg* family, while the glutamine is conserved only in the LPA receptors of the family. Other researchers hypothesize that the glutamine binds to the hydroxyl functional group on the glycerol backbone. This hypothesis parallels observations made in the S1P receptor models: that residue position contains a glutamate that is thought to interact with the positively charged ammonium group on sphingosine-1-phosphate. Our models indicate that the glutamine in LPA receptors binds to the phosphate head. This model of the binding pocket is equally plausible, even if the glutamate on S1P receptors interacts with the ammonium group, as there are significant differences in the structure S1P and LPA.⁴

Mutation studies performed on other *edg* receptors show that the positively charged residue located on helix 7 is also necessary for activation.^{3,5} Our predicted structure for LPA₂ and the binding site of LPA do not include that residue. This does not necessarily invalidate our structure. This work, as well as previous models for these receptors, focuses on modeling the binding of ligands into receptors, while mutation studies in lipid receptors only provide insight into activation. LPA receptor activation may depend on the charged residue at the extracellular end of helix 7, even if this residue is not located in the binding pocket. Molecular dynamics simulations discussed below demonstrate a strong salt-bridge between 7.36K and an aspartic acid on helix 6.

Interruption of this interaction in mutation studies, as opposed to an interaction between the ligand and 7.36K, could be responsible for inactivity of the mutant protein.

The glycerol backbone and lipid travel down toward the intracellular region between helices 3 and 6, with some contact with helices 4 and 5 (Figure 4.8). Our model contains a hydrogen bond between 4.63S and the hydroxyl functional group. In this hydrogen bond, the distance between heavy atoms is 2.97 Å. The carbonyl on the lipid accepts a hydrogen bond of length 2.90 Å from W¹⁹³ (Figure 4.9).

Table 4.3 presents a cavity analysis for the lipid and binding pocket. The interaction energies are based on neutral residues, so as not to overly weight the Coulombic interactions. Figure 4.10 shows the lipid and all residues with attractive interaction energies greater than 1.5 kcal/mol in stick form, while Figure 4.11 shows all residues within 5.0 Å of the ligand.

The binding energy between LPA and LPA₂ is -70.59 kcal/mol, again using neutral residues. This energy translates into an EC₅₀ that is orders of magnitude smaller than the experimentally determined value. Previous modeling attempts encountered similar challenges. Parrill *et al.* equate the docked energy score with the measure of Coulombic interactions.² If we only consider the Coulombic terms of binding energies and cavity interactions, our docked energies for all members of the LPA lipid family are within a few kcal/mol of previously published results for other LPA receptors.³ Using only the Coulombic term implies an assumption that the docking of the deprotonated phosphate head is primarily responsible for activation of lipid receptors. However, structure-activity relationship studies of LPA show that chain length also plays a role.^{3,5} The present models support this finding as the magnitudes of both the hydrogen-bonding

and van der Waals terms are very similar to, but larger than the Coulombic term. The hydrogen bonding and van der Waals terms from the cavity analysis are -20.22 and -18.85 kcal/mol respectively. For comparison, the Coulombic term from the cavity analysis is -13.77 kcal/mol.

The docking studies demonstrate that the structure contains a viable binding pocket for the prototypical LPA molecule, *cis*-18:1. Each functional group in LPA has an attraction to at least one residue in the binding pocket. Docking studies of two different ligand series provide further qualitative and quantitative structure validation. Examining the relative binding energies of LPA species with different chain lengths provides insight into the structure-activity relationships involving the lipid tail. The binding pocket surrounding the polar head group is explored through altering the functional groups on the second carbon. This second study also provides insight into the protein structure's sensitivity to the stereochemistry of the ligand.

4.4. Binding of Other Agonists

As noted in Chapter 3, we explore the binding of additional agonists beyond LPA *cis*-18:1. Experiments demonstrate binding selectivity changes with agonist chain length^{3,5}. Accordingly, we explore whether our model replicates this selectivity, as presented in Section 4.4.1. Investigations of the quantitative relationship between calculated binding energies and experimental measurements of protein activation further test the model. Section 4.4.2 presents these results.

4.4.1. Lipid Chain Selectivity

In addition to *cis*-18:1, the computational method evaluates seven other LPA species for their binding to LPA₂. Early studies on the structure-activity relationships between LPA receptors and lipid chain indicated selectivity for regioisomeric positioning of the tail (1-acyl vs. 2-acyl), chain length, and degree of saturation.⁵ These early experiments suggested that some LPA receptors were only activated by unsaturated species. More recent experiments indicate some of these results may have been an artifact of using insect cells that do not express all of the G proteins that couple to human LPA receptors.³ These experiments do not observe absolute selectivity based on the degree of lipid tail saturation, although efficacy is still influenced and chain-length selectivity is still apparent.

To explore the sensitivity of our predicted protein structure to ligand changes, the lowest energy structure for LPA *cis*-18:1 was modified to become one of the seven other LPA species shown in Table 4.4. Except in the case of LPA *trans*-18:1, lipid-tail torsions remain unaltered, and the coordinates of the phosphate head are unchanged. Following docking, scoring the bound ligand-protein complexes allows quantitative comparison of the various LPA ligands. Our analysis for ranking the docked energy of these complexes utilizes the cavity interaction energy. The lipid tails in these docked complexes are very similar to the tail identified through annealing dynamics and minimization for *cis*-18:1. Therefore, the strain energy should be constant among the ligands. Given that the calculation of solvation energy of a lipid in water shares no resemblance to physiologic processes, use of the cavity interaction energy instead of binding energy is appropriate.

According to Fujiwara *et al.*, the relative efficacies of the different LPA species follow the sequence: LPA 18:3 > LPA 18:2 \cong LPA *cis*-18:1 > LPA 18:0 > LPA 16:0 >> LPA 20:0.³ In this study, the predicted efficacy rankings for these ligands follows LPA 18:2 > LPA 18:3 > LPA 18:0 > LPA *cis*-18:1 > LPA 16:0 > LPA 20:0 (see Table 4.5). The present method most accurately predicts the worst activators, but the ordering of the best binders remains inconsistent with experimental results. Multiple factors may contribute toward this discrepancy. First, calculation of interaction energies only considers the enthalpic term and ignores entropy. The large number of torsional degrees of freedom, and the sole differences between these ligands being in the torsional structure, implies that the entropy term may not be negligible. Secondly, differentiating between good binders and poor binders (or activators, in this study) is easier than the fine distinctions needed to order attractive forces.

Since the coordinates of the phosphate head did not change until the binding pocket was minimized, overall the ligand position is nearly identical in all of the docked complexes. The positions of some of the side chains highlight the primary differences, as the residues within the binding pocket underwent side chain optimization after the new ligand was merged into the complex. As expected, the primary differences occur in the interactions between the lipid tails and the hydrophobic residues in the binding site. Table 4.6 lists all residues where the difference in the interaction energies is greater than 1.0 kcal/mol.

These results suggest that 3.46I/I¹²⁵ plays an important role in the physiology of LPA₂. LPA 20:0 extends down far into the barrel and forces the side chain of the isoleucine to rotate from the position seen in complexes containing better-activating

species. Even after rotating, there is still a strong repulsive interaction between the residue and the ligand. The interaction energy of 3.46I with LPA 20:0 is +3.44 kcal/mol, while it has a negative interaction energy with all other LPA species discussed. The one exception is the *trans* isomer of LPA 18:1, as 3.46I is not within 5.0 Å of that ligand. Not only does LPA 20:0 have a repulsive interaction with 3.46I, but that repulsion forces the hydrophobic chain of the ligand to shift within the pocket by approximately 0.75 Å. This shift weakens the interactions between L¹¹⁵/3.36L, while strengthening the interaction with S¹⁸⁸, which is conserved throughout the LPA receptors in the *edg* family. The side chain of that serine residue flips, putting the hydroxyl group pointing toward the ligand, as opposed to pointing toward helix 4, when LPA 20:0 is docked into the protein. Even though S¹⁸⁸ only weakly interacts with the prototypical LPA species, it may have significant structural importance. In fact, when the side chain points toward helix 4, hydrogen bonds are formed between the hydroxyl group and a histidine side chain, as well as the main chain of a cysteine residue in the second extracellular loop (Figure 4.12). From this analysis, three residues are identified as interesting targets for mutation studies: 3.46I, 3.36L, and S¹⁸⁸. Mutating S¹⁸⁸ to alanine can test whether the hydrogen bonds to helix 4 and EC2 are important, while mutating 3.36L and 3.46I to an assortment of other non-polar residues can provide evidence for the importance of the void space in the binding pocket. In particular, mutating them to Phe will provide evidence for which interactions are critical, as the binding pocket would be severely interrupted by that mutation.

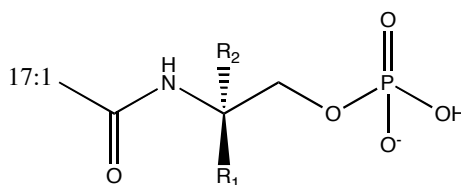
LPA *trans*-18:1 was also merged into our predicted structure for LPA₂. Fujiwara *et al.* did not examine the efficacy of the *trans* isomer³, but Bando *et al.* report an EC₅₀

of ~10 nM, which is the same value given for the *cis* isomer⁵ Our model predicts an interaction energy for the *trans* conformation that is only -1.1 kcal/mol higher in energy than the *cis* isomer. The binding pocket for the *trans* isomer, though, is significantly different from that seen for the other LPA species (Figure 4.13). As mentioned above, 3.46I is not within the binding pocket of the *trans* species. This supports the hypothesis that the side chain orientation of 3.46I is structurally important, as opposed to being important for activation. Without further study, it is difficult to conclude whether the *trans* LPA binding mode is viable. Of note, only LPA₂ has shown activation upon treatment with LPA *trans*-18:1.⁵

4.4.2. Selectivity About the Polar Headgroup

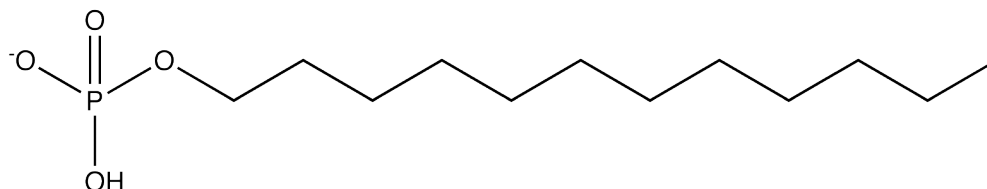
Examination of the binding pocket for the lipid headgroup requires branching out beyond the LPA family of lipids. The structure-activity relationships between the polar head group and the protein have been explored extensively, and quantitative comparisons are readily available. These experimental studies primarily focus on the glycerol backbone, as substitution of the phosphate head group eliminates activity.⁶

Herein we examine a series of *N*-acyl ethanolamide phosphatidic acid (NAEPA) derivatives as well as two short chain fatty acid phosphatidates, FAP-12 and FAP-10. Structure 4.1 shows the general form of the NAEPA derivatives.

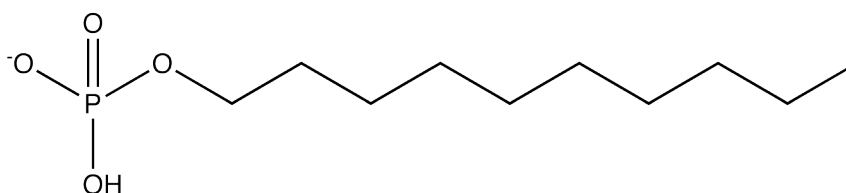


Structure 4.1 *N*-acyl ethanolamide phosphatidic acid, NAEPA

For various functional groups, we consider enantiomers where R_1 is the functional group and $R_2 = H$, and vice versa. Table 4.7 lists the functional groups and the EC_{50} for the set of NAEPA derivatives considered. The two short-chain fatty-acid phosphatidates FAP-12 (Structure 4.2) and FAP-10 (Structure 4.3) pictured below are fully saturated straight chain hydrocarbons beyond the phosphate head.



Structure 4.2 FAP-12



Structure 4.3 FAP-10

For the NAEPA derivatives, both enantiomers are built with those five substituents on the ethanolamide backbone. In each case, one of the enantiomers is a moderate to strong binder, while the stereoisomer is two to three times weaker.⁷ It should be noted that the NAEPA derivatives have one fewer carbon than the LPA species, but that the *cis* double bond is still at the ninth carbon.

For each pair of NAEPA-derived stereoisomers, we correctly pick which is the strong agonist and which is the weak one. We also correctly predict FAP-10 more

weakly activates LPA₂ than FAP-12. The predicted cavity-interaction energies are presented in Table 4.8. Previous models of LPA receptors have not explored selectivity for these ligands, nor have experiments identified unique residues responsible for the stereoselectivity. However, our technique allows exploration of both. Figure 4.14 shows the correlation between the predicted cavity interaction energies and experimental results. When all tested ligands are examined, the correlation coefficient was 0.55. A tendency to overestimate the attractive interactions is seen, which more significantly impacts the predictions for weak agonists. This tendency can also be seen in the qualitative analysis of different LPA species described in Section 4.4.1.

Since the construction of these ligands is based on perturbation of the binding mode for LPA *cis*-18:1, the binding pockets are very similar. Because the *cis* double bond in the NAEPA series shifts toward the phosphate head relative to its placement in LPA *cis*-18:1, the lipid tail does not have an identical conformation to that of the endogenous ligand (Figure 4.15). FAP-12 and FAP-10, though, do have identical conformations for the shared sections of the backbone and tails.

The results from this study suggest that stereoselectivity results partly from the formation of a hydrogen bond to S¹⁶⁸/4.63S and interactions with Q108/3.29Q. Of the species in this study, the enantiomeric pair VPC31139 and VPC31180 shows one of the largest differences in efficacy and the largest difference in interaction energies. Qualitatively the binding pockets look similar (Figure 4.16), excepting the hydrogen bond formed between S¹⁶⁸ and the carbonyl oxygen of the carbomethyl substituent. The interaction energy from this hydrogen bond is -4.51 kcal/mol, almost 3 kcal/mol stronger than the interaction between VPC31180 and S¹⁶⁸.

One of the other significant adjustments in the binding pocket involves Q¹⁰⁸, one of the residues implicated by mutation studies of LPA₁ and S1P₁. VPC31139 forms a hydrogen bond 5.24 kcal/mol stronger with Q¹⁰⁸ than VPC31180, with a net difference in interactive energies of 3.43 kcal/mol. These results are only suggestive, though, as the magnitude of these differences varies with ligand pairs.

Residue Y¹⁸⁹ consistently shows significant differences in its interactions between strong agonists and weak agonists. For all of the ligands in the NAEPA series, the stronger agonist creates an interaction with Y¹⁸⁹ that is at least 1.3 kcal/mol stronger than the interaction between the weak agonist and the tyrosine residue. This tyrosine does not interact with the functional group on the glycerol backbone, but with the phosphate head. One of the trends seen in the NAEPA series is that molecules with smaller substituents are generally stronger agonists than those with larger functional groups.⁷ Our data suggest that this results, in part, from the placement of the Tyr side chain relative to the variable functional group. Larger substituents force an increase in the distance between the hydroxyl group on the tyrosine and the phosphate head of the ligand. VPC12109 has an ethyl functional group on the second carbon and a distance between the tyrosine and phosphate head of 3.34 Å. The phosphate head of VPC12086, which has a methyl substituent, is only 2.80 Å from Y¹⁸⁹. Shifts in both the ligand position and in the residue position contribute to the change in distance.

The binding pockets for FAP-10 and FAP-12 illuminate interactions critical to activation. The ligand phosphate head interacts with Y¹⁸⁹, R¹⁰⁷, and Q¹⁰⁸. The interaction seen between LPA *cis*-18:0 and W¹⁹³ is not essential for activation, as neither FAP-12 or

FAP-10 interact with the Trp. The role of S¹⁶⁸ in activation remains unclear, as there are still weak interactions between that residue and ligands lacking the glycerol backbone.

The different efficacies of FAP-12 and FAP-10 also elucidate the importance of L¹¹⁵/3.36L for activation. The additional chain length on FAP-12 increases the residue-ligand interaction for L¹¹⁵. Activation may be particularly sensitive to the position of this residue, as changes in the polar head group lead to small shifts in the positioning of the lipid tail, and all of the strong agonists in the NAEPA series interact more strongly with that residue than with their weaker, stereoisomeric counterpart.

The data presented here support our postulated structure, as most of the experimental results can be explained through examination of the predicted binding pocket. Docking LPA mimetics of varying efficacy illuminates some of the important residues involved in activation/binding in LPA₂. Three residues within the binding pocket have potential as new mutation candidates for experimental study: Y¹⁸⁹, L¹¹⁵, and I¹²⁵. The position of Y¹⁸⁹ changes upon docking different stereoisomers of the NAEPA derivatives, which may explain the stereoselectivity seen experimentally. FAP-10 and FAP-12 have interaction energies with L¹¹⁵ that mirror their efficacy in activating LPA₂. The location of L¹¹⁵ within the binding pocket determines the difference in interaction energies, as FAP-10 does not reach as far into the binding site. The isoleucine residue suggested as a mutation candidate interacts less with the weak agonist LPA 20:0 than it does with the rest of the LPA species studied.

4.5. Molecular Dynamics

Long time-scale molecular dynamics are used to relax the complex as completely as possible and to illustrate the role of solvent in ligand binding. This analysis focuses on qualitative observations made over the course of a dynamics run lasting just longer than one nanosecond. The total energy of the system is mostly equilibrated after 160 ps, and is fully equilibrated after 300 ps. A plot of temperature vs. time shows identical equilibration times (data not shown). Section 4.5.1 describes how the protein structure changes over the course of the dynamics, while Section 4.5.2 notes how the binding pocket and the ligand are altered over time. Structural comparisons are made between the structure at $t=0$ and the structure with the lowest overall energy over the course of the dynamics (seen at $t=833$ ps). The protein-ligand complex structure at $t=0$ is different than the structure discussed above since it has been minimized with the water and lipid membrane as solvent. The protein structure at $t=0$ is very similar to the protein structure discussed above. The ligand, on the other hand, has a very different conformation.

4.5.1. Changes in Protein Structure

The reorganization of the helices is the primary change seen in the protein structure over the course of the dynamics. The RMSD between the structures is 5.35 Å when accounting for side chain equilibration but only 4.47 Å when examining the alpha carbons of the backbone. The helices move much closer to one another from their starting positions. Helices 1, 6, and 7 move toward the center of the barrel, helix 5 moves closer to helix 4, which moves closer to helix 2 (Figure 4.17). These shifts in position are not due solely to the translational degrees of freedom. Helix 4 and 7 undergo significant

rotation, as shown in Figure 4.18. Overall, helix 7 undergoes the most significant changes.

As expected, the helices no longer behave as rigid bodies. Animation of the molecular dynamics shows helices raveling and unraveling. These transformations occur at the ends of helices or in the middle, depending on the helix and the time step. The molecular dynamics provide evidence that the TM prediction for helix 3 is incorrect. The two turns at the extracellular end of helix 3 unravel during the dynamics, while the bottom (intracellular region) curls into a helix. If this observation is correct, the homology models of the LPA receptors also predict the same residues at the top of helix 3 to be part of the transmembrane domain instead of in the extracellular loops.^{2,4,8}

The molecular dynamics provide insight into some of the inconsistencies between the homology model developed by others and our predicted model. The lysine residue on helix 7 (7.36K), which has been implicated in mutation studies of other *edg* receptors, may play a critical role due to its interaction with helix 6, rather than interactions with the ligand. As noted above, helix 7 rotates considerably over time. Once the structure has equilibrated, that lysine residue forms a stronger salt bridge with an aspartic acid on helix 6 (6.58D) than is seen prior to the dynamics run. The length of the hydrogen bond changes from 2.89 Å in the beginning structure to 2.69 Å in the lowest energy structure. The arginine residue at the EC end of helix 5 (R¹⁸⁷), though, never moves into the binding pocket after over one nanosecond of dynamics. Throughout this entire dynamics time course, the arginine is completely solvated by water. As the phosphate head of the ligand interacts with one charged residue and multiple other polar residues and is solvent

accessible, no other charged residue is inherently necessary for binding of the phosphate functional group.

4.5.2. Changes in the Ligand and Binding Pocket

The structure of both the ligand and the binding pocket change considerably through minimization and over the course of the dynamics simulation. The RMSD between the ligand the start of the dynamics and in the lowest energy structure is 3.33 Å, although upon overlaying the ligand the RMSD is only 1.86 Å. The most significant changes are seen around the double bond in the lipid tail and in the position of the hydroxyl group on the glycerol backbone (Figure 4.19).

Within the binding pocket, the ligand shifts toward helices 6 and 7 at the extracellular end of the binding pocket, but the tail moves closer to helix 5 (Figure 4.20). Many residues on helix 7 that do not show up in the docking studies appear within the binding site after molecular dynamics. The phosphate head of the ligand also sits closer to the EC region after the dynamics. Between the compression of the bundle and the shifting of the ligand, the binding pocket for LPA is significantly tighter than before the dynamics. The polar head group of the ligand, along with the polar residues surrounding it, is shown in Figure 4.21, while Figure 4.22 depicts the non-polar residues surrounding LPA *cis*-18:0. Tyr and Trp fall into both categories and are shown in both figures. Figure 4.23 illustrates the general types of interactions, *i.e.*, polar or non-polar, throughout the binding site. If one considers Trp polar or non-polar depending on the local environment, only one polar residue lies in the hydrophobic portion of the 4.0 Å binding pocket. The hydroxyl group of that Ser, S¹⁹⁶, does not interact with the ligand.

Instead, it forms a hydrogen bond with the backbone of V¹⁹². One Leu residue, L¹⁰⁶, resides in the hydrophilic end of the binding site, but it interacts with the relatively non-polar glycerol backbone of LPA.

Although quantitative analyses of binding in the post-MD protein are not available, the picture of the binding pocket clearly indicates that a longer lipid would disrupt the bottom of the hydrophobic pocket. Two residues, V²⁰⁷ and F²⁵⁰, cradle the end of the lipid tail. Of the two, docking studies described earlier only identify F²⁵⁰ as part of the binding site.

Possible mutation candidates are derived from the docking studies discussed above. In particular, we hypothesize that S¹⁸⁸ creates structurally important hydrogen bonds. After molecular dynamics, only one of those hydrogen bonds remains, so it is less likely that the position of the hydroxyl group on S¹⁸⁸ provides structural integrity to the binding site. Molecular dynamics clarify that another suggested mutation candidate, I¹²⁵, might not play a role in differentiating between LPA species. The isoleucine residue does not reside within 5.0 Å of the ligand after MD simulations. Instead, V²⁰⁷ and F²⁵⁰ are excellent candidates for mutation. Mutating F²⁵⁰ to Tyr and/or V²⁰⁷ to Phe will decrease the void space at the end of the lipid tail, which should prohibit LPA 20:0 and, perhaps, LPA 18:0 from activating the receptor.

Molecular dynamics enhances the validity of L¹¹⁵ and Y¹⁸⁹ as mutation candidates. Experimentally, FAP-12 has a stronger influence on LPA₂ than FAP-10. L¹¹⁵ interacts with FAP-12 more strongly than it does with FAP-10. That leucine residue sits at the same level within the protein as the double bond in LPA does. Mutating L¹¹⁵ to

Phe would diminish the width of the binding pocket significantly, creating a more severe chain-length dependence than is seen in the wild-type receptor.

If Y¹⁸⁹ is critical for binding the polar head group of LPA, mutating it to Ala should significantly increase the EC₅₀ of the receptor. Previously, we suggested that the position of Y¹⁸⁹ contributes to the stereoselectivity seen in the NAEPA derivatives. To test this, mutating the aromatic Tyr to a more flexible polar residue, such as Gln or Asn, should restore activity of the weaker stereoisomer.

In conclusion, molecular dynamics simulations add significant insight into the binding mode of LPA *cis*-18:0 in LPA₂. The majority, but not all, of the residues in the binding pocket after MD are predicted by the docking studies, but the docking studies do predict some false-positive residues. Further analysis of the dynamics will provide quantitative information about selectivity of the receptor and the significance of entropy in GPCR activation.

4.6. Tables and Figures

NT (31)	MVIMGQCYNETIGFFYNNSGKELSSHWRPK
TM 1 (30)	DVVVVALGLTVSVLV LLTN LLVIAAIASNR
IC 1 (8)	RFHQPIYY
TM 2 (23)	LLGNLAAAD L FAGVAYLFLMFHT
EC 1 (13)	GPRTARLSLEGWF
TM 3 (24)	LRQGLLDTSL T ASVATLLAIAVER
IC 2 (19)	HRSVMAVQLHSRLPRGRVV
TM 4 (23)	MLIVGV V VAA L GLGLLPAHSWHC
EC 3 (13)	LCALDRCSRMAPL
TM 5 (26)	LSRSYLAVWALSSLL V FLLMVAVYTR
IC 3 (30)	IFFYVRRRVQORMAEHVSCHPRYRETTLSLV
TM 6 (27)	KTVVVIILGAFVVC W TPGQVVLLLDGLG
EC 3 (5)	CESCN
TM 7 (26)	VLAVEKYFLLLAE A NSLVNA A AVYSCR
CT (53)	DAEMRRTFRRLCCACLRQSTRESVHYTSSAQGGASTRIMLPENGHPLMDSTL

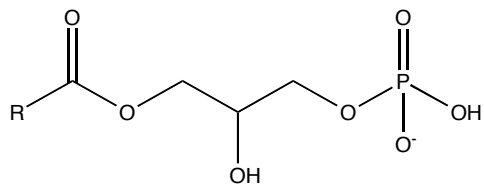
Table 4.1 The sequence of LPA₂, broken up into domains predicted by TM2ndS. The calculated hydrophobic center is in bold, and the most highly conserved residue in each helix, used in the Ballesteros and Weinstein numbering scheme, is underlined. No residue is underlined for helix 5, since there is no proline in that helix. The residue that aligns with that highly conserved proline in bovine rhodopsin varies based on the alignment method used, so the numbering scheme for that helix is highly ambiguous. The number of residues in each segment is given in parentheses next to the section identifier. IC represents intracellular loops and EC indicates extracellular loops.

Donor Helix	Donor Residue		Acceptor Helix	Acceptor Residue		D-A Distance (Å)
1	29-ASN	ND2	7	26-ARG	O	3.09
2	16-TYR	OH	7	7-TYR	OH	2.95
5	26-ARG	NH1	3	21-ALA	O	2.75
5	26-ARG	NH1	3	22-VAL	O	2.83
3	24-ARG	NH1	5	23-VAL	O	2.79
3	24-ARG	NH2	5	24-TYR	O	3.27
3	2-ARG	NH2	7	7-TYR	OH	3.06
4	19-HSE	NE2	5	4-SER	OG	2.96
5	3-ARG	NH2	4	23-CYS	SG	3.34
7	6-LYS	NZ	6	24-ASP	OD1	2.53
7	6-LYS	NZ	6	24-ASP	OD1	2.53
7	6-LYS	NZ	6	24-ASP	OD2	2.68
7	6-LYS	NZ	6	24-ASP	OD2	2.68

Table 4.2 The inter-helical hydrogen bonds in the predicted structure of LPA₂ are presented here. The numbering of the residues is independent for each helix. The model of LPA₂ developed in this work contains a strong inter-helical hydrogen-bonding network.

Residue		VdW	Coulomb	H-Bond	NonBond
ARG	107	6.43	-3.91	-9.9	-7.37
TRP	193	2.55	-2.41	-4.51	-4.38
TYR	189	-0.53	-2.75	-0.68	-3.95
GLN	108	2.74	-1.25	-5.14	-3.65
LEU	111	-3.35	-0.17	0	-3.52
LEU	115	-3.3	-0.02	0	-3.31
SER	118	-2.22	-0.12	0	-2.33
ARG	177	-1.78	-0.15	0	-1.93
LEU	122	-1.82	0.04	0	-1.78
VAL	119	-1.69	0.01	0	-1.69
CYS	253	-1.45	-0.01	0	-1.45
SER	168	0.86	-2.28	0	-1.42
THR	121	-1.4	0.00	0	-1.4
LEU	203	-1.4	0.01	0	-1.38
SER	188	-0.68	-0.63	0	-1.31
LEU	164	-1.12	-0.02	0	-1.13
TYR	279	-1.01	-0.00	0	-1.02
ALA	249	-0.95	0.01	0	-0.95
LEU	185	-1.11	0.2	0	-0.91
ILE	125	-0.89	0.02	0	-0.88
LEU	199	-0.91	0.04	0	-0.87
PHE	250	-0.83	0.00	0	-0.83
SER	114	-0.89	0.05	0	-0.83
LEU	282	-0.8	0.03	0	-0.77
CYX	178	-0.66	-0.07	0	-0.73
VAL	192	-0.64	-0.08	0	-0.72
SER	196	-0.44	-0.09	0	-0.53
VAL	200	-0.53	0.02	0	-0.51
CYX	271	-0.41	-0.06	0	-0.47
TRP	254	-0.45	-0.00	0	-0.45
SER	270	-0.19	-0.18	0	-0.37
Total		-18.85	-13.77	-20.22	-52.84

Table 4.3 A cavity analysis of LPA *cis*-18:1 docked into LPA₂. The units are in kcal/mol. Due to the size of the ligand, the binding pocket for LPA is significantly larger than the binding pockets seen in other GPCRs.⁹⁻¹²



Ligand	Details of Saturation
LPA <i>cis</i> -18:1	<i>Cis</i> at Δ^9
LPA 18:0	Saturated
LPA 16:0	Saturated
LPA 20:0	Saturated
LPA 18:2	<i>Cis</i> at Δ^9 and Δ^{12}
LPA 18:3	<i>Cis</i> at Δ^9 , Δ^{12} and Δ^{15}
LPA <i>trans</i> -18:1	<i>Trans</i> at Δ^9

Table 4.4 The structures of all LPA species docked into LPA₂ are shown here.

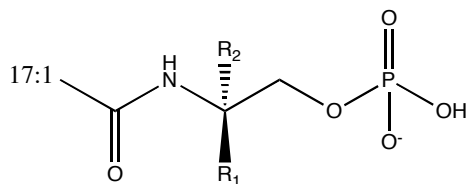
Ligand	Total Cavity Interaction Energy (kcal/mol)
LPA 18:2	-56.475
LPA 18:3	-55.974
LPA 18:0	-54.685
LPA <i>cis</i> -18:1	-52.84
LPA <i>trans</i> -18:1	-51.741
LPA 16:0	-51.157
LPA 20:0	-48.164

Table 4.5 The total cavity interaction energy for each species of LPA, as calculated with the DREIDING¹³ force field, is provided here. Although our ranking order does not exactly match that observed in experiments,³ the model created in this work does differentiate between good activators and poor activators, based on their interaction energies.

	LPA 18:2	LPA 18:3	LPA 18:0	LPA 18:1 cis	LPA 18:1 trans	LPA 16:0	LPA 20:0
LPA 18:2		THR 121	LEU 115 SER 188	ARG 177	SER 118 VAL 119 THR 121 LEU 122 LEU 203	LEU 115 THR 121	LEU 115 ILE 125 SER 188 ALA 249
LPA 18:3			LEU 115 SER 188	ARG 177	SER 118 VAL 119 LEU 122 LEU 203 PHE 250 TRP 254	LEU 115 SER 118	LEU 115 ILE 125 SER 188
LPA 18:0		THR 121		ARG 177	SER 118 VAL 119 THR 121 LEU 203	THR 121	ILE 125 ALA 249
LPA cis- 18:1	ARG 107	ARG 107	ARG 107 LEU 115 SER 188		ARG 107 SER 118 VAL 119 THR 121 LEU 122 LEU 203	ARG 107 LEU 115 THR 121	ARG 107 LEU 115 ILE 125 SER 188 ALA 249
LPA trans- 18:1	SER 114 LEU 282 ALA 286 VAL 290	SER 114 LEU 282 ALA 286 VAL 290	SER 114 SER 188 LEU 282 ALA 286 VAL 290	ARG 177 LEU 282 ALA 286 VAL 290		SER 114 ALA 249 LEU 282 ALA 286 VAL 290	SER 114 LEU 115 SER 188 ALA 249 LEU 282 ALA 286 VAL 290
LPA 16:0			SER 188	ARG 177	SER 118 VAL 119 LEU 122 LEU 203		ILE 125 SER 188
LPA 20:0		THR 121		ARG 177	SER 118 VAL 119 LEU 122 LEU 199 LEU 203	THR 121	

Table 4.6 A comparison of important residues in the binding pocket of each ligand.

Within each block, the residue listed has a more attractive interaction with the ligand denoted by the row than it does with the ligand denoted by the column. Residues highlighted in red are not within 5.0 Å of the ligand indicated in the column header.



Functional Group		R ₁ functionalized, R ₂ = H (EC ₅₀)	R ₂ functionalized, R ₁ =H (EC ₅₀)
Methylene Hydroxy ⁷		VPC31143 (116.5 nM)	VPC31144 (2645 nM)
Carbomethyl ⁷		VPC31139 (29.2 nM)	VPC31180 (3461 nM)
Methylene Amino ⁷		VPC12178 (50.3 nM)	VPC12048 (8250 nM)
Methyl ⁷	CH ₃	VPC12086 (18.3 nM)	VPC12101 (>5000 nM)
Ethyl ⁷		VPC12109 (161.9 nM)	VPC12115 (4280 nM)

Ligand	EC ₅₀
LPA <i>cis</i> -18:1 ⁷	6.8 nM
FAP-12 ¹⁴	700 nM
FAP-10 ¹⁴	3700 nM

Table 4.7 The ligands examined as LPA₂ agonists and their efficacies

Ligand	Cavity Interaction Energy	Log(EC₅₀)
VPC12086	-46.16	-7.74
VPC12101	-38.00	N/A
VPC31139	-47.41	-7.53
VPC31180	-40.32	-5.46
VPC12178	-40.76	-7.3
VPC12048	-37.84	-5.08
VPC31143	-41.72	-6.93
VPC31144	-37.70	-5.58
VPC12109	-42.24	-6.79
VPC12115	-35.36	-5.37
FAP-12	-28.29	-6.15
FAP-10	-24.05	-5.43
LPA <i>cis</i> 18:1	-52.84	-8.17

Table 4.8 The predicted cavity interaction energies, along with the experimentally measured efficacies. The top-listed ligand of each pair is the stronger activator. For each pair, we correctly predict which is the stronger agonist.

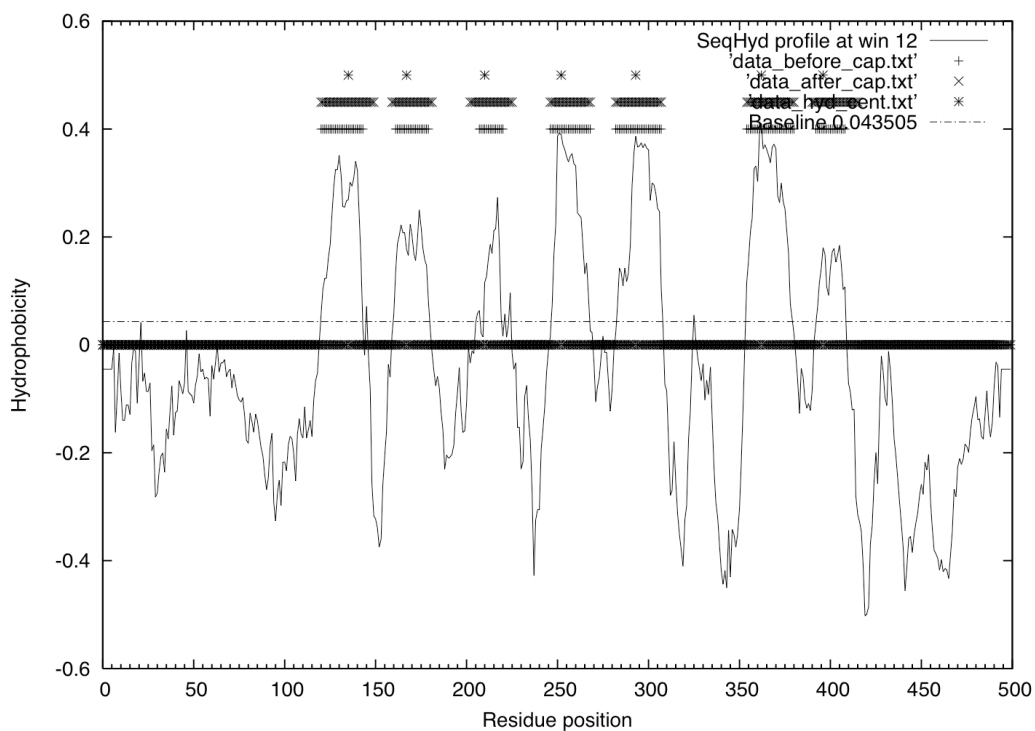


Figure 4.1 A plot of the hydrophobicity of LPA₂. Areas above the dashed x -axis indicate lipid-soluble regions that we predict to be transmembrane helices. Seven distinct peaks are seen, although the baseline was adjusted to resolve helices 4 and 5.

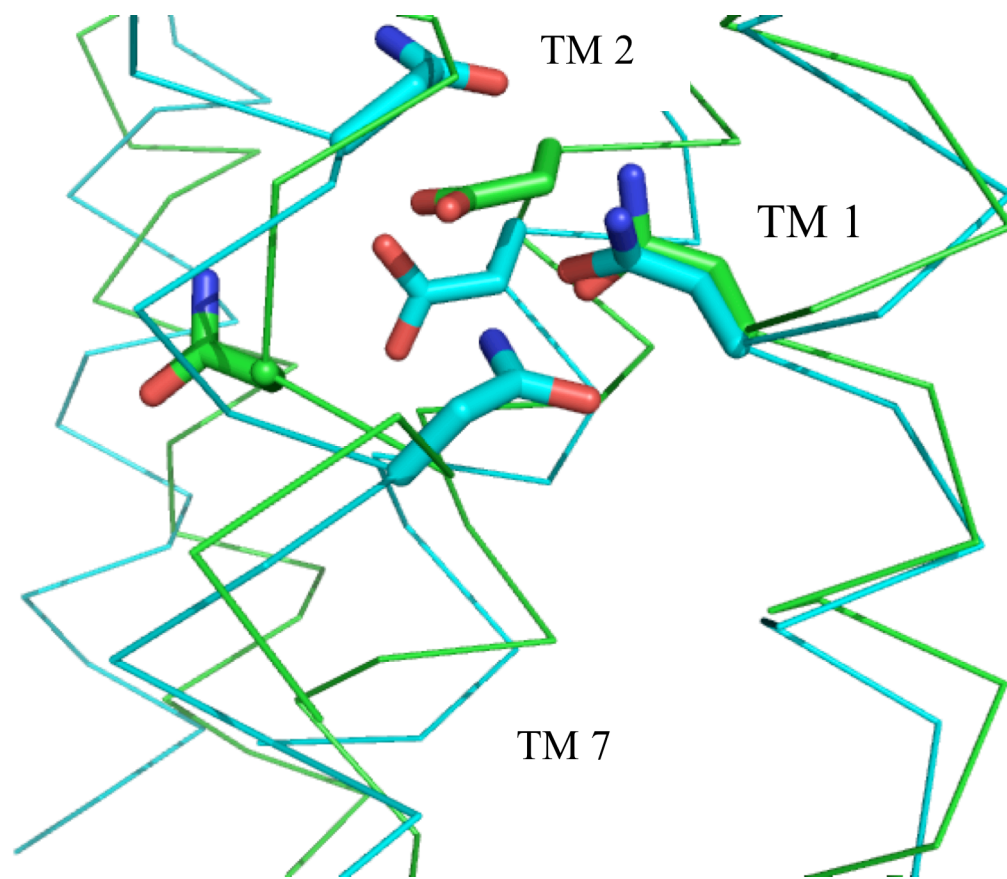


Figure 4.2 A comparison of the TM 1-2-7 hydrogen-bonding network in bovine rhodopsin (green) and human LPA₂ (blue). There is significant overlap between the two proteins on helices 1 and 2, while helix 7 of LPA₂ is rotated clockwise (looking from the extracellular region) from the position of helix 7 in rhodopsin. This hydrogen-bonding network evolved organically, *i.e.* without any bias from homology data. The structure of rhodopsin is from the PDB database, accession number 1F88.

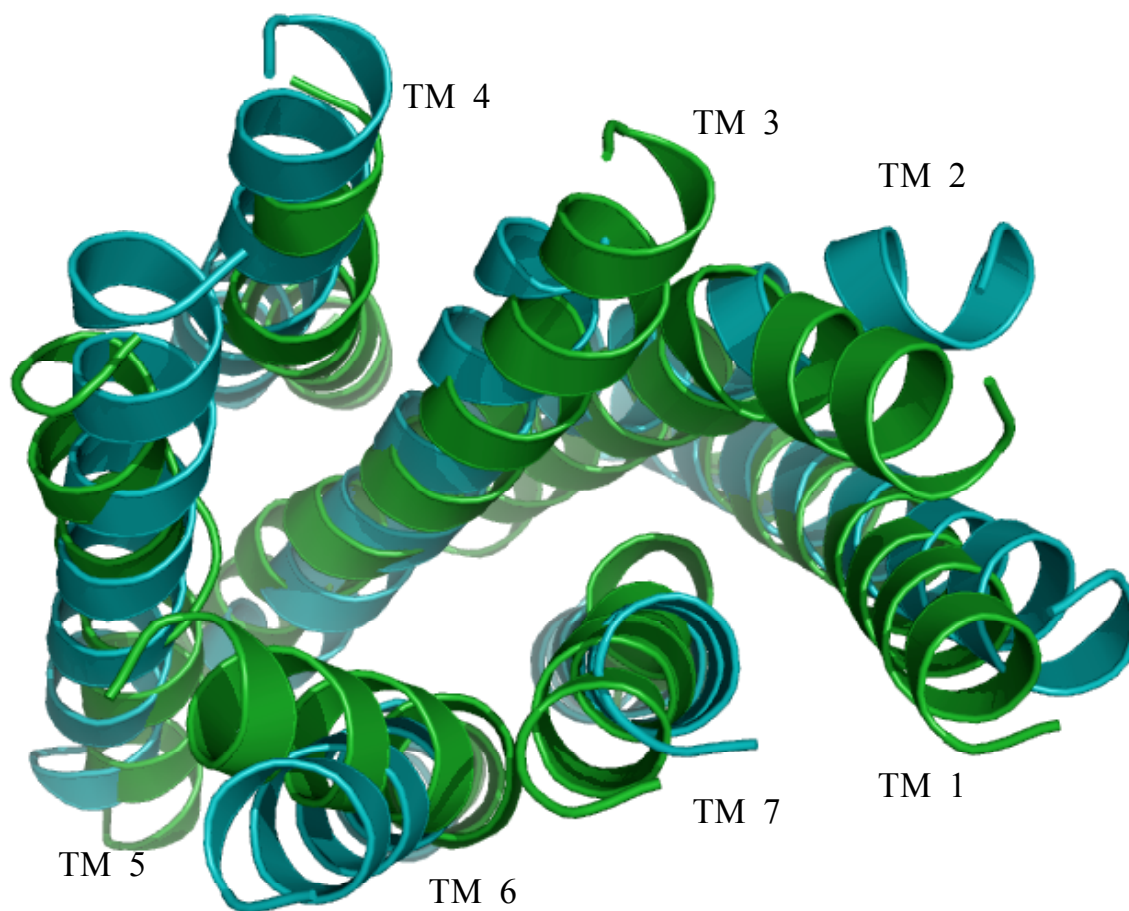


Figure 4.3 An overlay of the TM region backbones in bovine rhodopsin (green) and human LPA₂ (blue). Despite using a common topology to align the tilts of the helices, our modeling methods allow for significant relaxation.

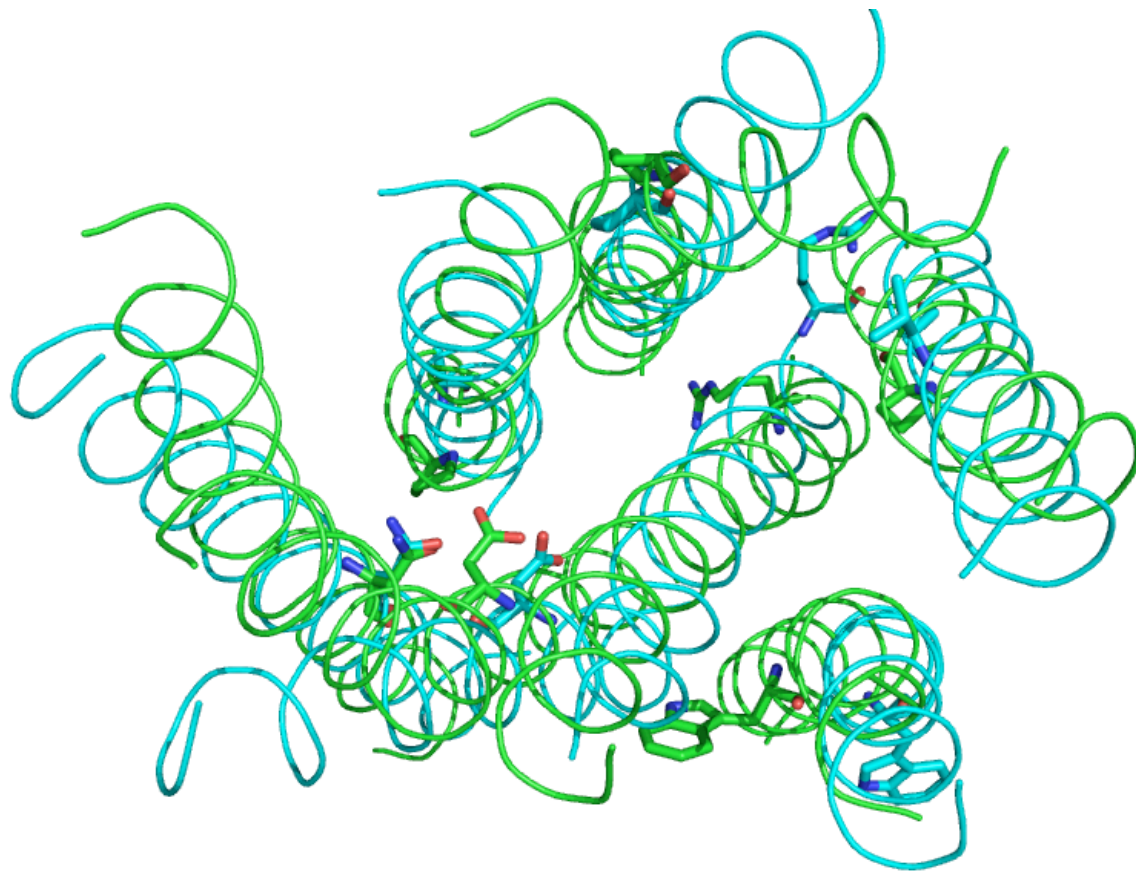
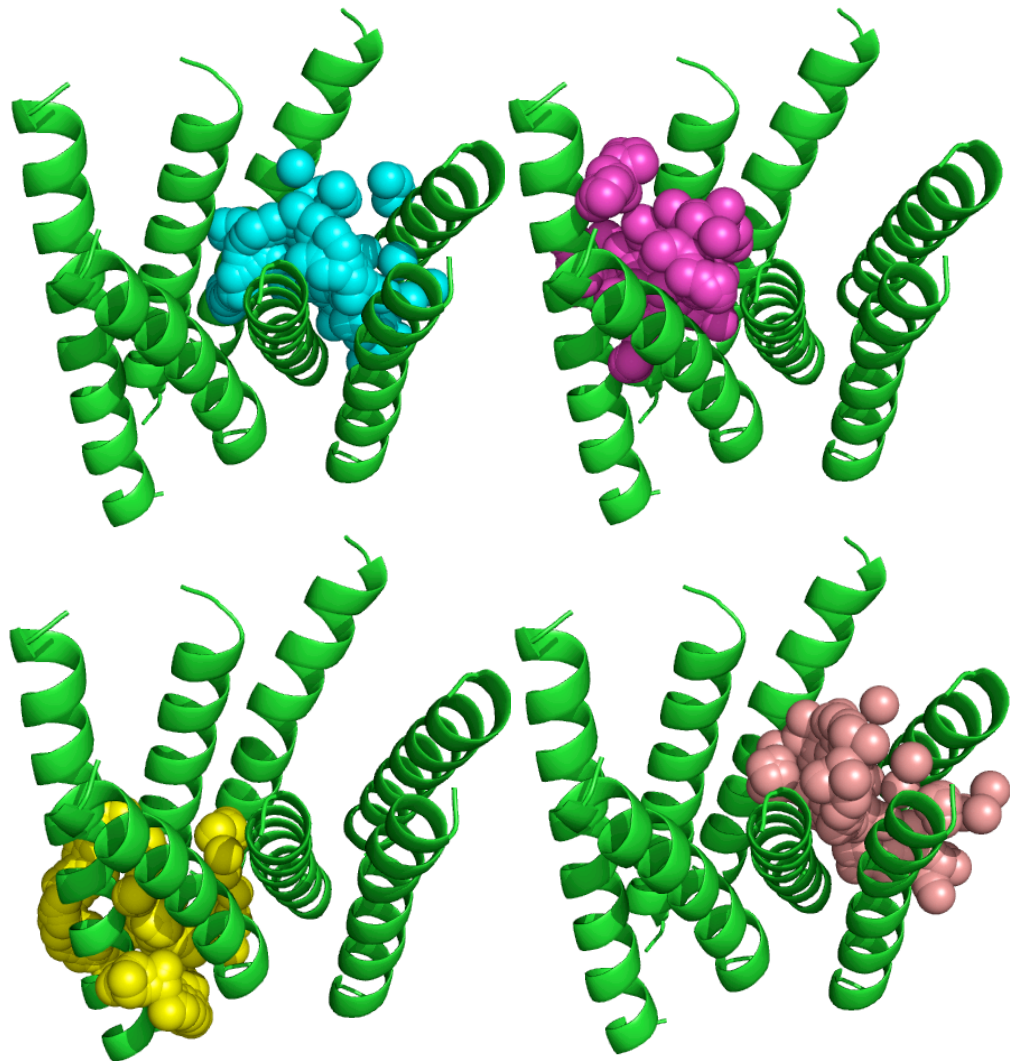


Figure 4.4 The transmembrane regions of bovine rhodopsin (green) and human LPA₂ (blue). The most highly conserved residues in each TM helix are shown as sticks, and the C-alpha backbone as a ribbon. Despite not using any experimental data for orienting the helices with respect to translation or rotation, most of the conserved residues show very good overlap. With regards to translation, six of the seven helices are well matched. Helix 5 of LPA₂ is lifted toward the EC region, relative to bovine rhodopsin. Helices 3, 4, 5, and 7 have different rotations in LPA₂ than in rhodopsin, although the difference in TM3 is minimal. These differences are of note since some of these helices (3, 4, and 5) are involved in ligand binding in both proteins.



(Figure 4.5 continues on the next page.)

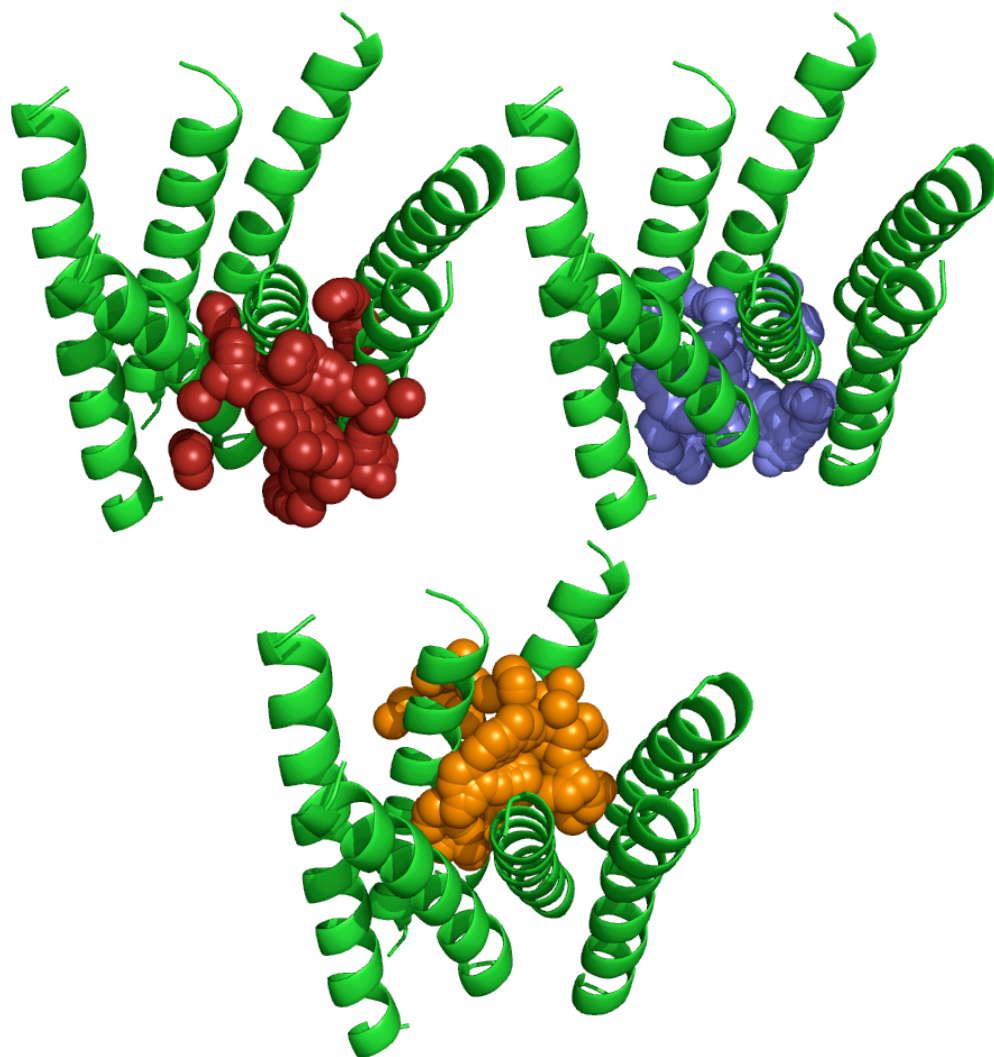


Figure 4.5 Each panel shows one sphere set obtained from the PASS algorithm, progressing. Six of the seven sphere sets primarily covered space inside the bundle, but all seven were used to insure full sampling of the protein space. The protein is oriented such that the left most helix is helix 1, and the numbering increases in a counter-clockwise fashion. The extracellular region would lay at the top of each panel.

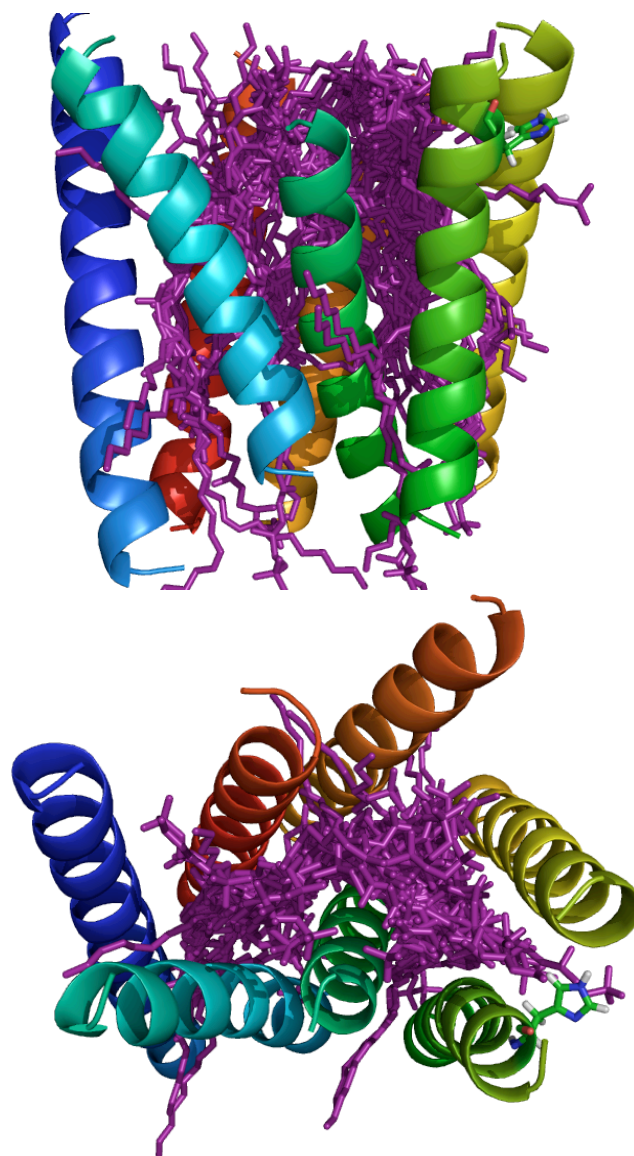


Figure 4.6 A visual depiction of the sampling of the TM region during docking, from the side in the top panel and from the extracellular region in the bottom panel. The N-terminus of the protein is in blue and the C-terminus is in red. Note that the ligand conformations shown in purple are a subset of all conformations docked into the protein. This subset passed a buried surface criterion ($\geq 70\%$) and was limited to the 30 lowest energy structures from each sphere set (shown in Figure 4.5). Even with the limitations on this set, there is near complete sampling of all void space in the barrel.

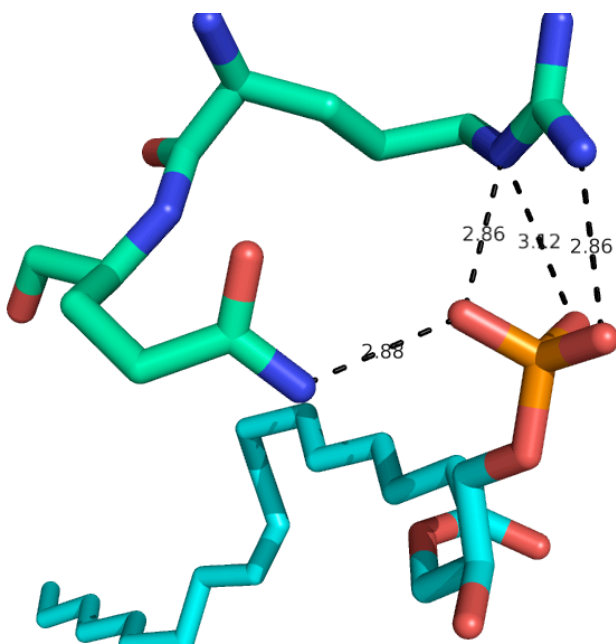


Figure 4.7 A picture of the binding pocket for the phosphate head of LPA *cis*-18:1 docked into LPA₂. There are very strong attractive interactions between 3.28R and 3.29Q.

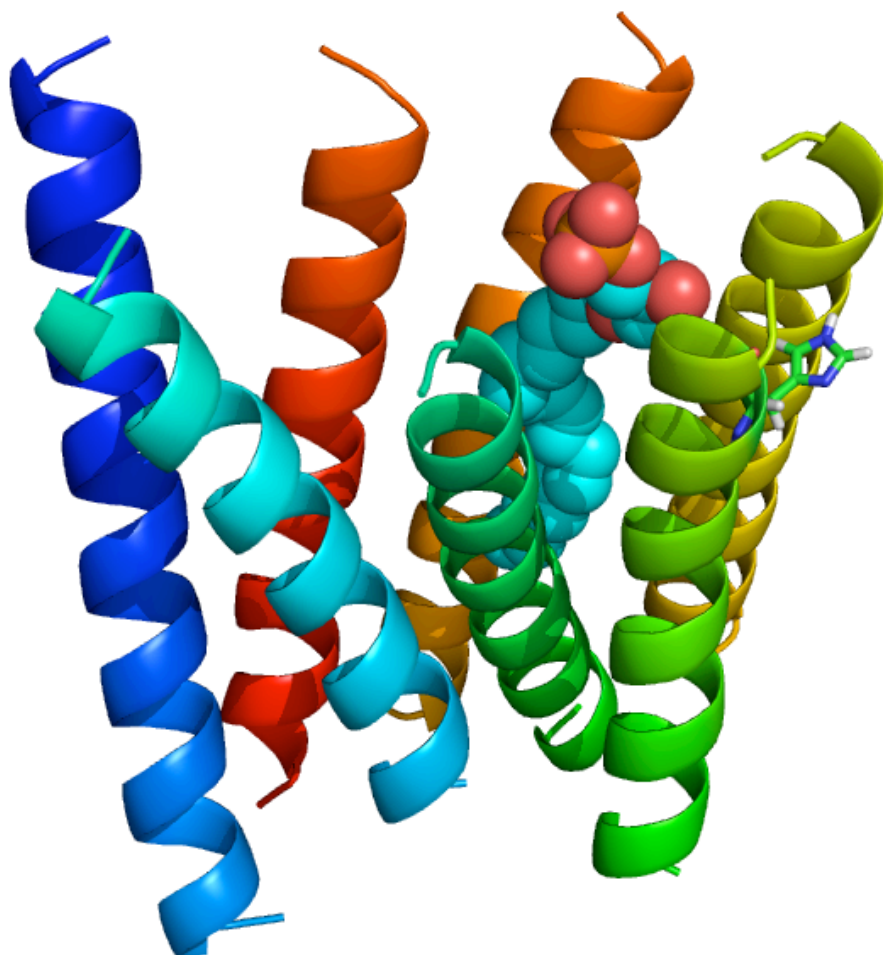


Figure 4.8 A picture of LPA (spheres) from the lowest energy complex in the TM region.

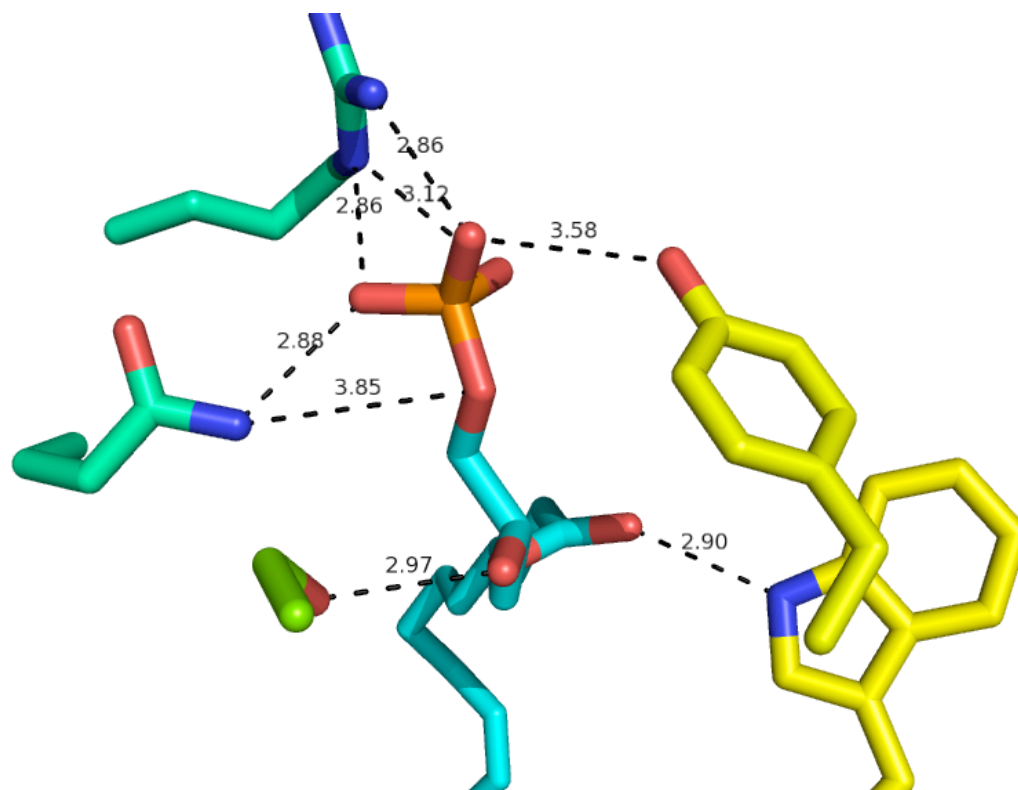


Figure 4.9 LPA docked into LPA₂. All functional groups on LPA have made some polar contact with the protein. Almost all of the acceptor-donor distances are less than 3 Å, indicating a very good fit of the ligand into the pocket.

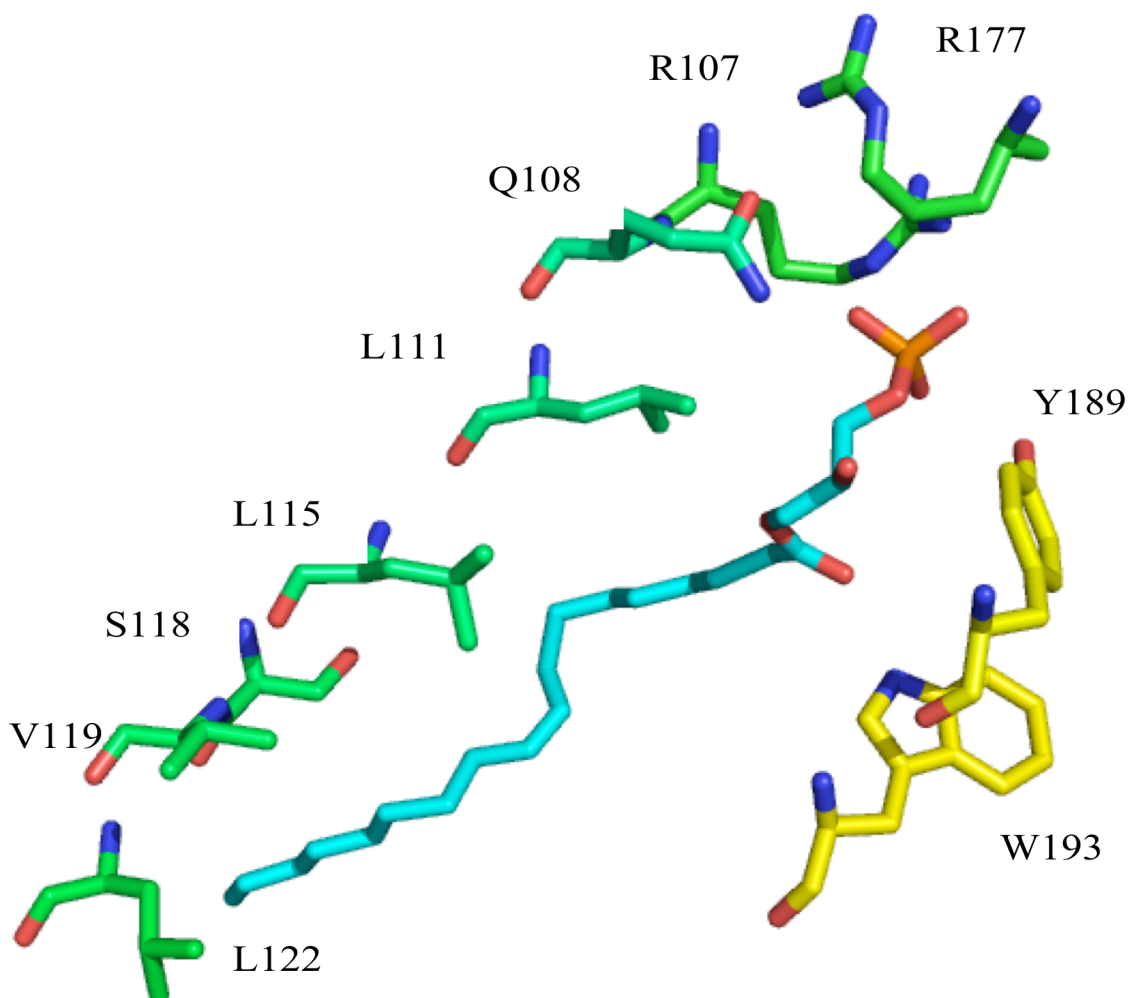


Figure 4.10 There are ten residues within the binding pocket of LPA in LPA₂ that contribute more than 1.5 kcal/mol to the attractive interaction energy between the two species. Each polar functional group on the ligand creates a hydrogen bond with one of the residues within 3.0 Å. The hydrophobic tail is supported by a series of non-polar residues along TM3.

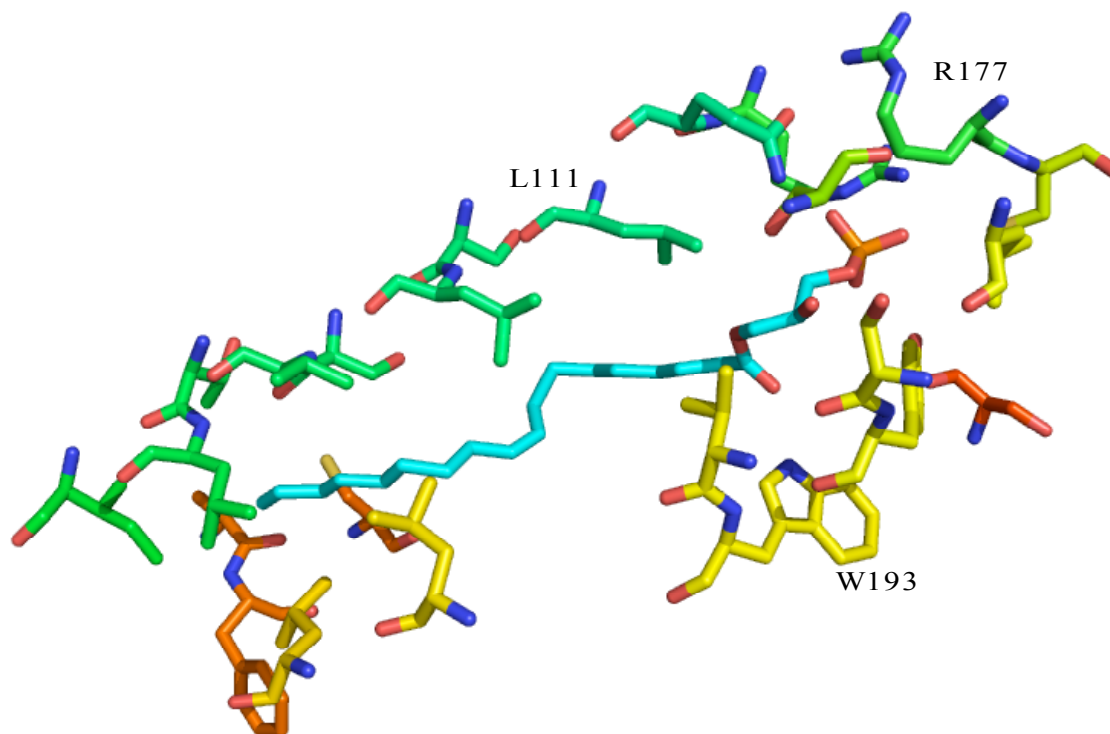


Figure 4.11 LPA *cis*-18:1 fits snugly into the 5.0 Å binding pocket in LPA₂. The majority of the strong attractive van der Waals interactions are between TM3 and the lipid tail. The strong Coulombic interactions and hydrogen bonds are found around the phosphate head, near the extracellular region. Helix 3 is colored green and helix 5 is yellow. A few residues are labeled to orient the viewer.



Figure 4.12 LPA 20:0 shifts within the binding pocket in LPA₂ so that the serine residue pictured in the center flips to face inward toward the ligand. When that flip occurs, multiple hydrogen bonds that could be structurally important are broken, which may contribute to the poor activation of LPA 20:0.

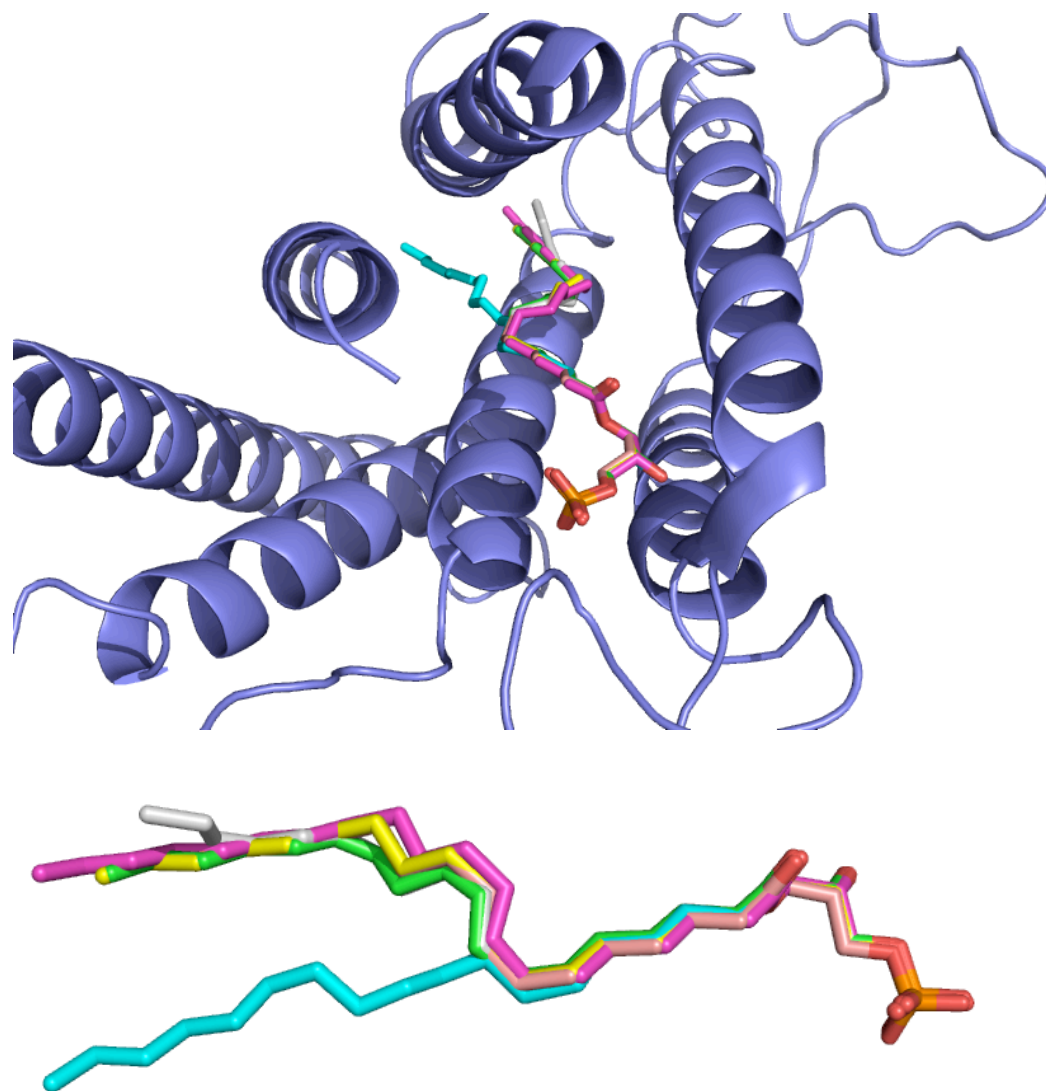


Figure 4.13 The *trans* isomer of LPA (cyan) has a different binding mode than the other LPA species examined. The top panel shows the position of the ligands within the protein, while the bottom panel is a detailed picture of the ligands overlaid. One can also see that the tail for LPA 20:0 (magenta) extends further down in the binding pocket than the other tails.

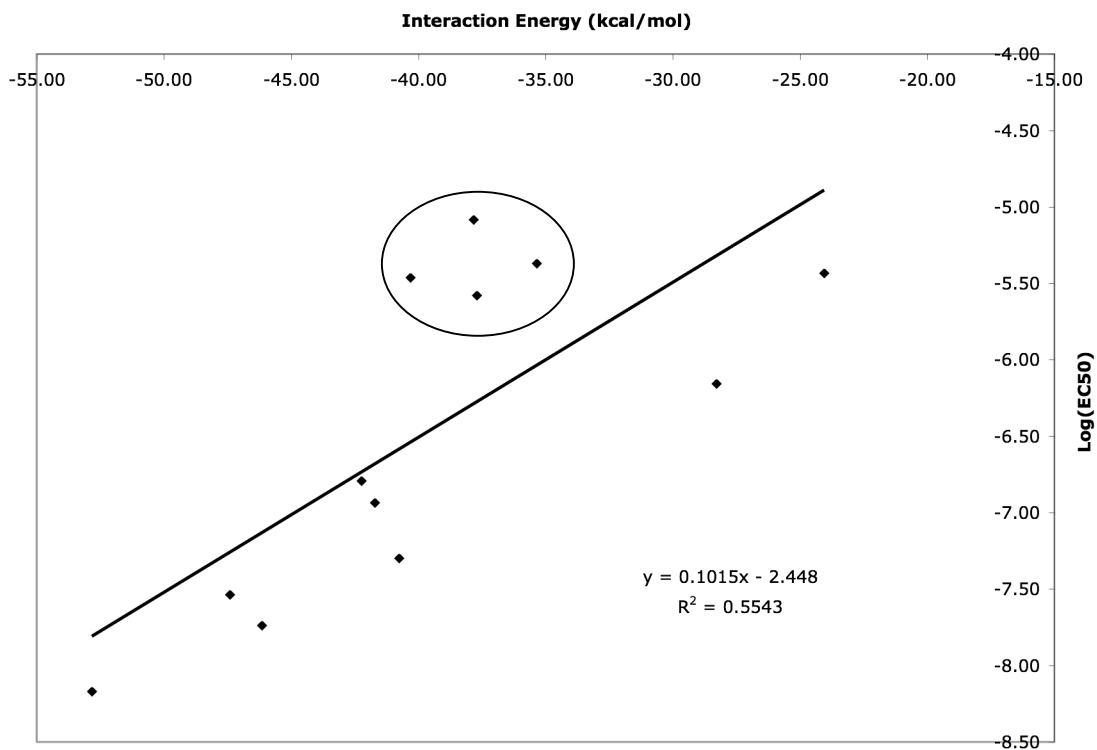


Figure 4.14 The correlation between cavity interaction energies and experimentally measured efficacies. The four points located in the circle show weak agonism in experiments. The line is the linear regression for all 12 data points. The equation for the line is $y = 0.1015x - 2.448$, and has a correlation coefficient of 0.55. When the four points in the oval are removed from the data set, the correlation coefficient rises to 0.93 and the equation $y = 0.0884x - 3.4313$ describes the linear regression.



Figure 4.15 A general picture of the NAEPA derivatives inside the protein is presented in the top panel. The bottom panel is a detailed look at the relative conformations of the tails for the different ligand series. The ligand depicted in orange is VPC31143, green is FAP-12, and magenta is LPA *cis*-18:1.

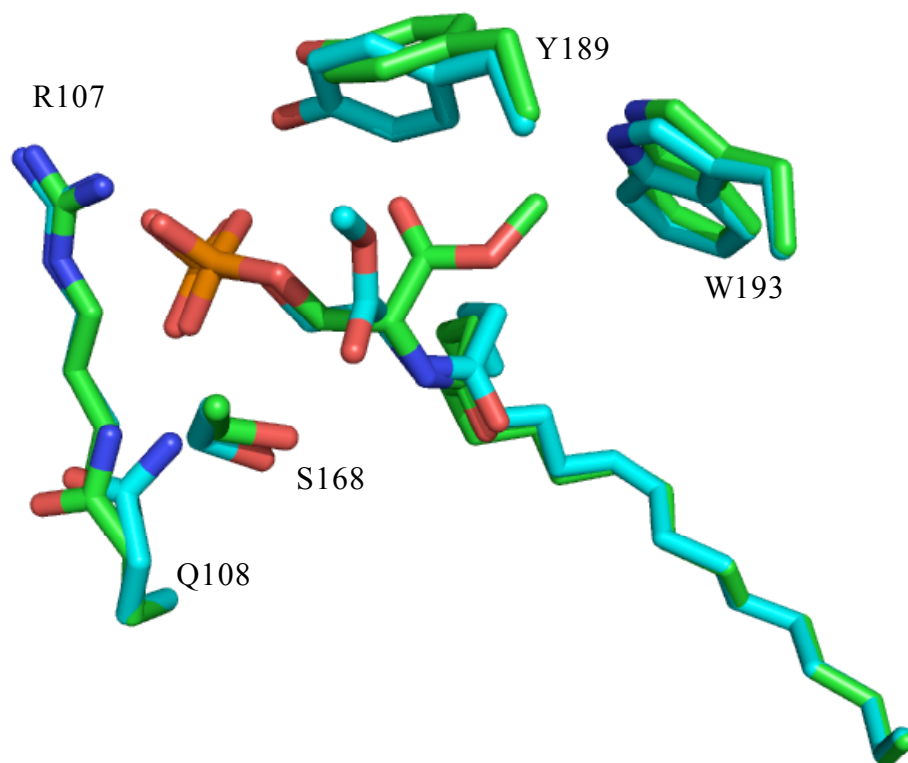


Figure 4.16 VPC31139 (cyan) and its enantiomer VPC31180 (green) are depicted. Polar residues that differ in each binding site are also shown. The subtle shifts in Q¹⁰⁸, S¹⁶⁸, and Y¹⁸⁹ create significant differences in interaction energies that affect the activity of each stereoisomer.

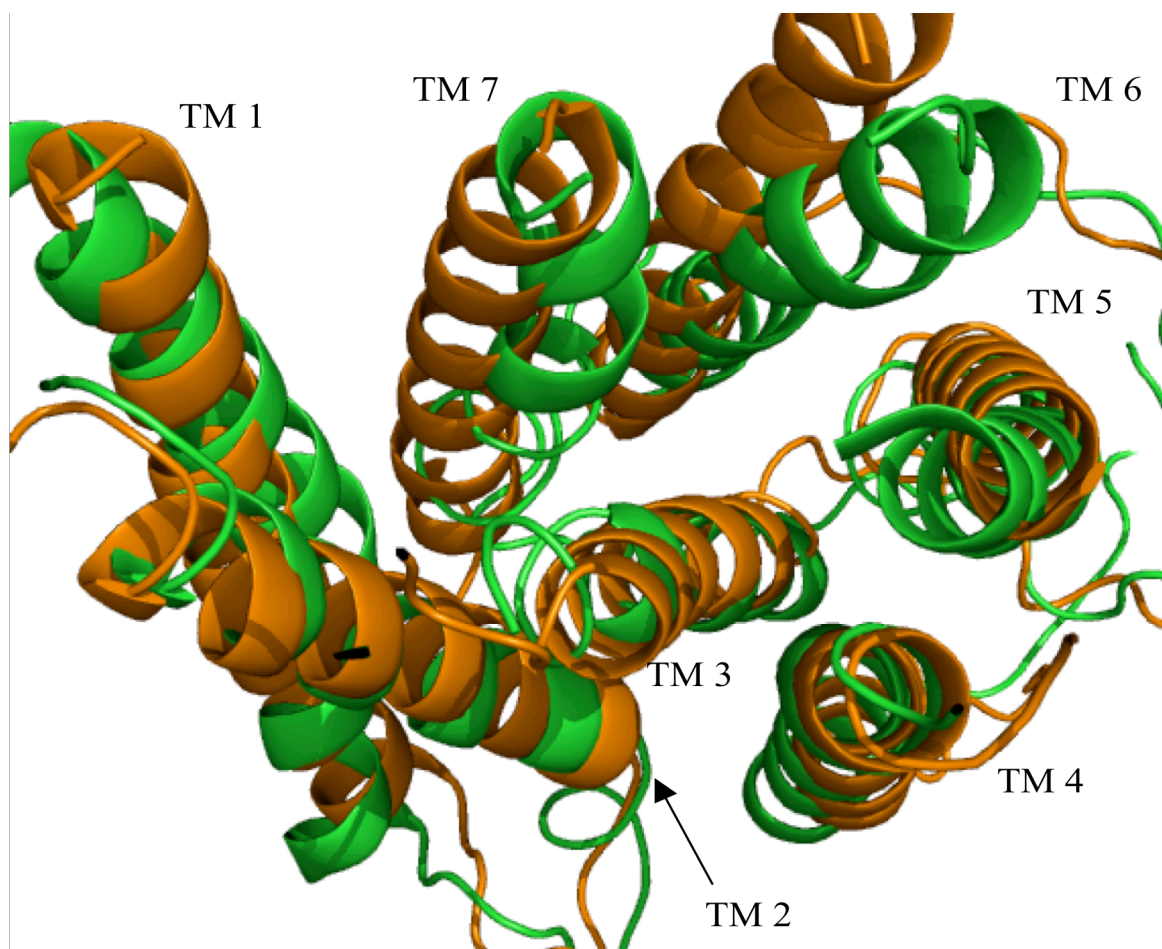


Figure 4.17 An overlay of the predicted structures for LPA₂, before (orange) and after (green) long time-scale molecular dynamics, shows how the helix positions change over time. Generally, the helices move closer together, both because of translation and because of rotations of the helices.

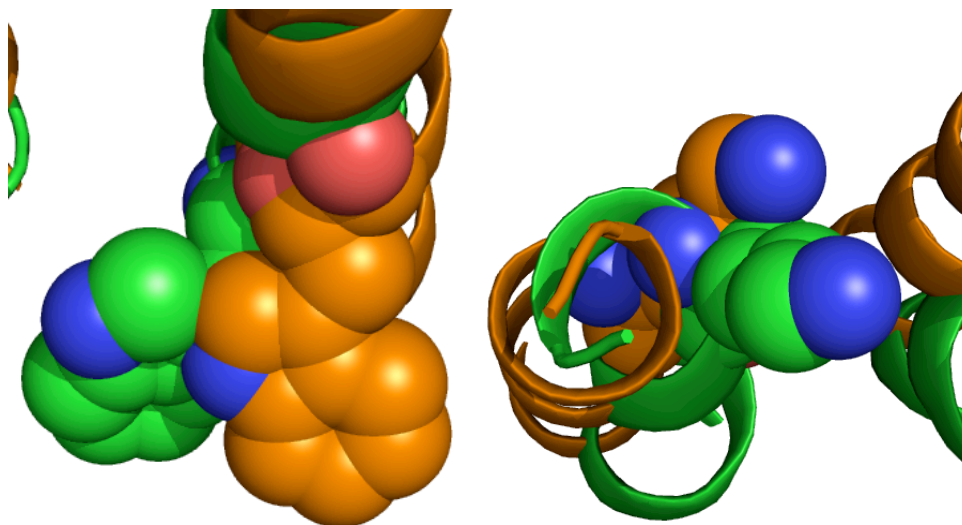


Figure 4.18 Helices 4 (left panel) and 7 (right) undergo substantial rotation over the course of molecular dynamics. (Before: orange; After: green.) A lysine implicated in homology models is shown on helix 7, and the highly conserved Trp on helix 4 is shown.

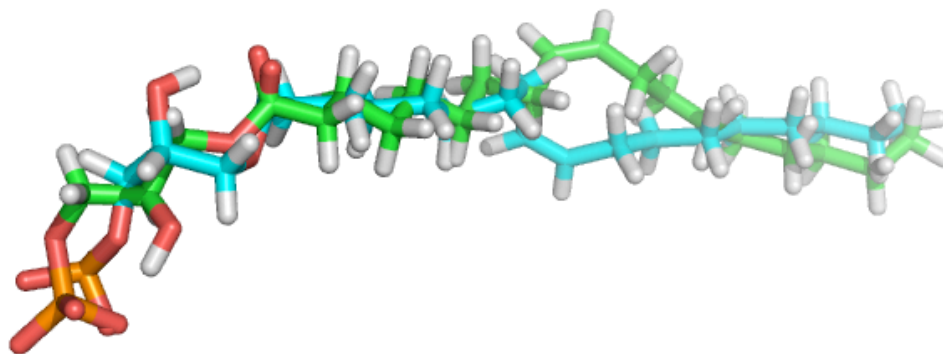


Figure 4.19 The overlay of LPA *cis*-18:1, before (green) and after (cyan) molecular dynamics, shows how the structure of the ligand changes over the course of time.

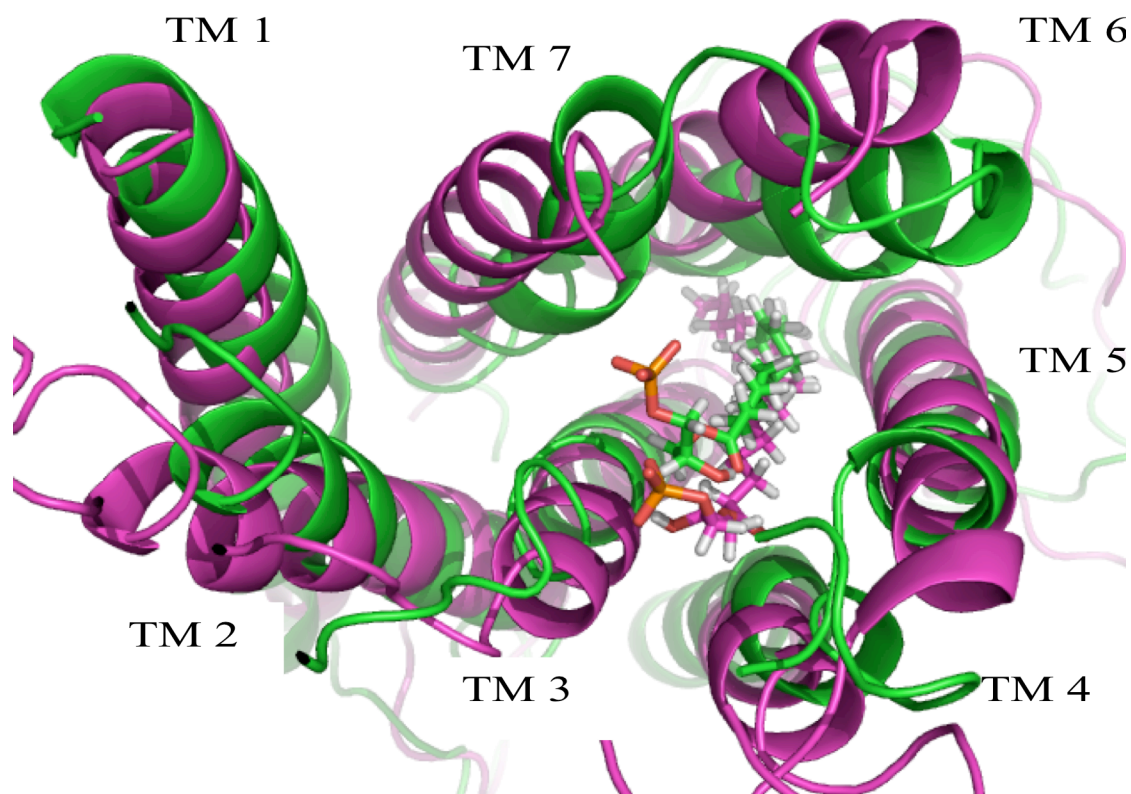


Figure 4.20 The ligand shifts toward helices 6 and 7 over the course of the dynamics. The structure before dynamics is shown in purple, and after dynamics in green.

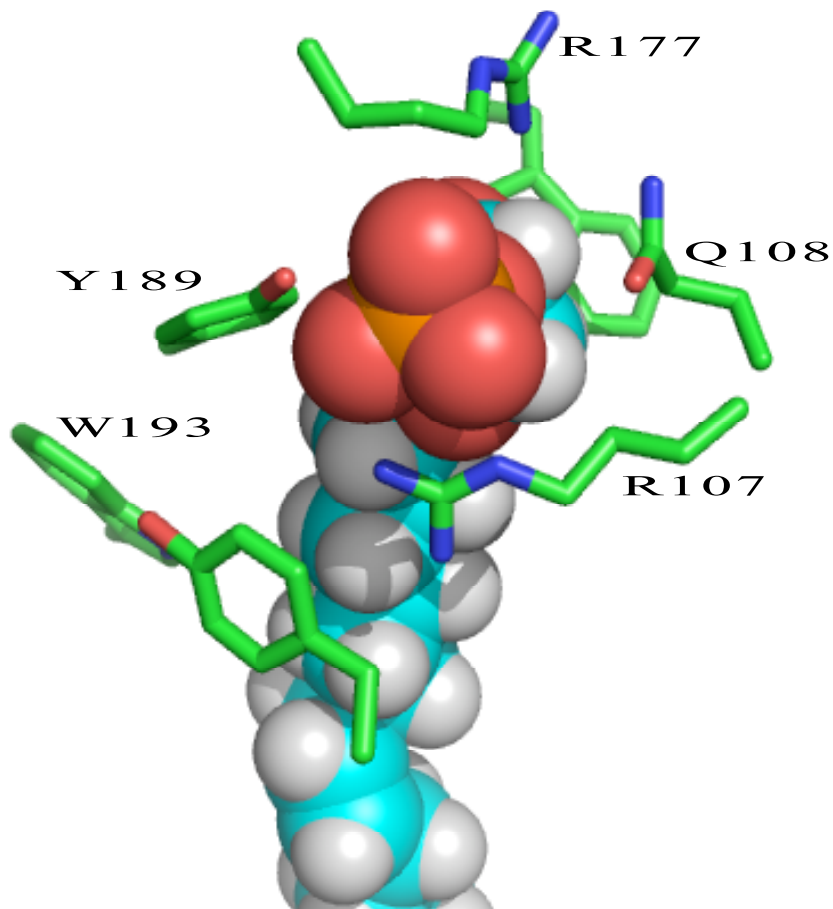


Figure 4.21 The fit of the polar head group into the 4.0 Å binding pocket after MD is similar to what is seen before molecular dynamics. The two residues implicated in homology models combined with mutation studies, R107 and Q108, both lie in the binding pocket. After MD, Q108 is closer to the hydroxyl group than before MD. Y189 remains an important, although untested, part of the binding pocket. The hypothesis that Y189 confers stereoselectivity on the binding pocket remains plausible. Mutation of Y189 to Phe will illuminate the importance of the Y189-phosphate hydrogen bond.

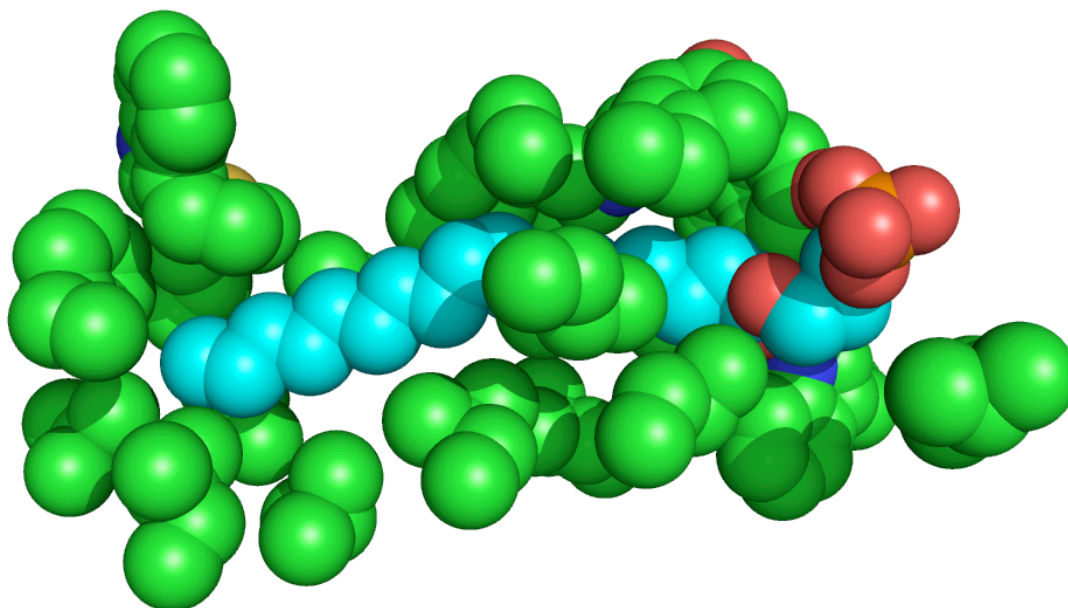


Figure 4.22 During molecular dynamics, the hydrophobic binding pocket collapses around the ligand, creating a tighter fit. The main-chain atoms and hydrogens have been removed from the picture for clarity. Very little void space exists at the end of the lipid tail, creating a natural limitation for chain length of the ligand tail.

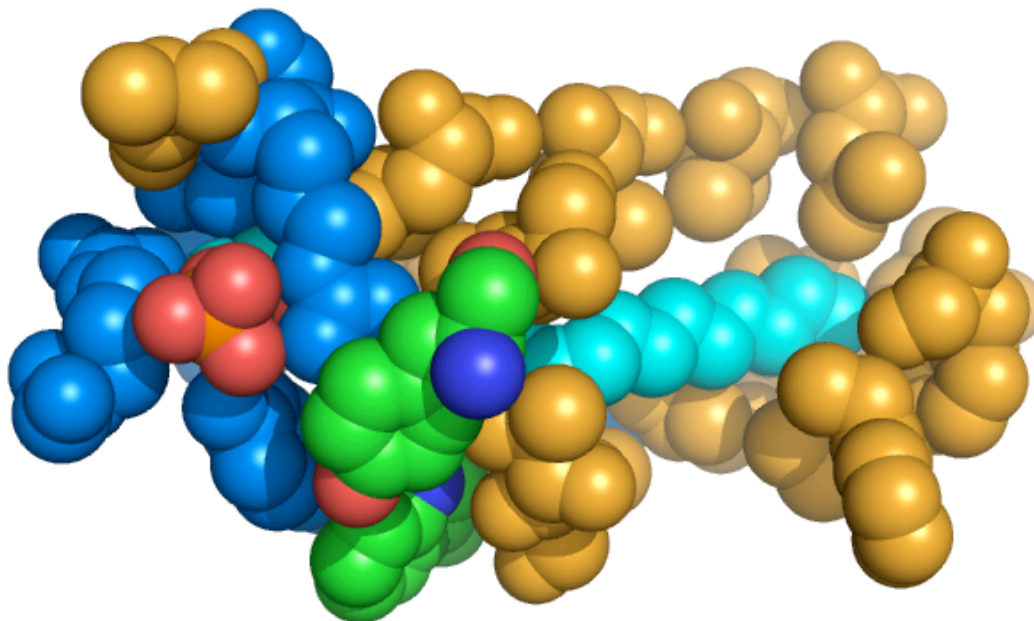


Figure 4.23 Non-polar residues are colored gold and polar residues are colored blue. Non-polar residues, almost exclusively, pack around the lipid tail, while the polar head group is surrounded by polar functional groups. A Leu fits into the hydrophilic pocket to interact with the glycerol backbone. In the hydrophobic region, there is a Ser residue (behind the lipid tail in this figure). The hydroxyl group, though, interacts with main-chain atoms and not the ligand. A Tyr residue and a Trp (both colored by atom, with green carbons) sit at the border between the hydrophobic and hydrophilic ends.

4.7. References

- (1) Okada, T.; Sugihara, M.; Bondar, A.-N.; Elstner, M.; Entel, P.; Buss, V. *Journal of Molecular Biology* **2004**, *342*, 571-583.
- (2) Bautista, D. L.; Baker, D. L.; Wang, D.; Fischer, D. J.; Brocklyn, J. V.; Spiegel, S.; Tigyi, G.; Parrill, A. L. *Journal of Molecular Structure-Theochem* **2000**, *529*, 219-224.
- (3) Fujiwara, Y.; Sardar, V.; Tokumura, A.; Baker, D.; Murakami-Murofushi, K.; Parrill, A.; Tigyi, G. *Journal of Biological Chemistry* **2005**, *280*, 35038-35050.
- (4) Wang, D. A.; Lorincz, Z.; Bautista, D. L.; Liliom, K.; Tigyi, G.; Parrill, A. L. *Journal of Biological Chemistry* **2001**, *276*, 49213-49220.
- (5) Bandoh, K.; Aoki, J.; Taira, A.; Tsujimoto, M.; Arai, H.; Inoue, K. *Febs Letters* **2000**, *478*, 159-165.
- (6) Tigyi, G.; Parrill, A. L. *Progress in Lipid Research* **2003**, *42*, 498-526.
- (7) Heise, C. E.; Santos, W. L.; Schreihofner, A. M.; Heasley, B. H.; Mukhin, Y. V.; Macdonald, T. L.; Lynch, K. R. *Molecular Pharmacology* **2001**, *60*, 1173-1180.
- (8) Parrill, A. L. *Biochemical Society Transactions* **2005**, *33*, 1366-1369.
- (9) Hummel, P.; Vaidehi, N.; Floriano, W. B.; Hall, S. E.; Goddard, W. A. *Protein Science* **2005**, *14*, 703-710.
- (10) Hall, S. E.; Floriano, W. B.; Vaidehi, N.; Goddard, W. A. *Chemical Senses* **2004**, *29*, 595-616.
- (11) Freddolino, P. L.; Kalani, M. Y. S.; Vaidehi, N.; Floriano, W. B.; Hall, S. E.; Trabanino, R. J.; Kam, V. W. T.; Goddard, W. A. *Proceedings of the National Academy of Sciences of the United States of America* **2004**, *101*, 2736-2741.
- (12) Vaidehi, N.; Floriano, W. B.; Trabanino, R.; Hall, S. E.; Freddolino, P.; Choi, E. J.; Zamanakos, G.; Goddard, W. A. *Proceedings of the National Academy of Sciences of the United States of America* **2002**, *99*, 12622-12627.
- (13) Mayo, S. L.; Olafson, B. D.; Goddard, W. A., III *Journal of Physical Chemistry* **1990**, *94*, 8897-8909.
- (14) Virag, T.; Elrod, D. B.; Liliom, K.; Sardar, V. M.; Parrill, A. L.; Yokoyama, K.; Durgam, G.; Deng, W. L.; Miller, D. D.; Tigyi, G. *Molecular Pharmacology* **2003**, *63*, 1032-1042.